

AD-A136 378

RELIABILITY STUDIES OF CERAMIC CAPACITORS(U) MISSOURI  
UNIV-ROLLA H U ANDERSON ET AL. JUL 83 N00014-82-K-0294

1

UNCLASSIFIED

F/G 9/1

NL

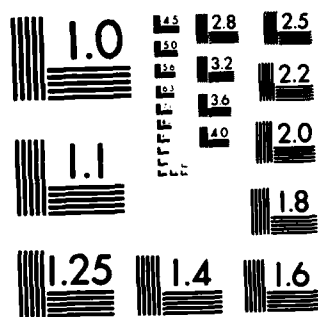
END

DATE

FILED

84

DTIC



MICROCOPY RESOLUTION TEST CHART  
NATIONAL BUREAU OF STANDARDS-1963-A

A136378

12

RELIABILITY STUDIES OF CERAMIC CAPACITORS

Progress Report  
for period of  
July 1, 1982 to June 30, 1983

H. U. Anderson and D. E. Day  
University of Missouri-Rolla  
Rolla, Missouri 65401

July 1983

DTIC

DEC 29 1983

Prepared for the  
Office of Naval Research  
Contract No. N00014-82-K-0294

**DISTRIBUTION STATEMENT A**

Approved for public release;  
Distribution Unlimited

DTIC FILE COPY

83 12 25 062

# CONTENTS

	Page
Introduction . . . . .	3
Current Status, Achievements, and Future Studies . . . . .	3
Current Program . . . . .	5
Specimen Preparation and Compositions . . . . .	5
Compound Preparation and Fabrication . . . . .	11
Measurements . . . . .	12
Injection Mechanisms in Solids . . . . .	28
Thermally Stimulated Current Measurements . . . . .	47
Cooperative Programs . . . . .	66
University of Missouri-Rolla/Draper Laboratory Program . . . . .	66
University of Missouri-Rolla/Pennsylvania State University Program . . . . .	66
References . . . . .	68

Accession For	
NTIS GRA&I	<input checked="" type="checkbox"/>
DTIC TAB	<input type="checkbox"/>
Unannounced	<input type="checkbox"/>
Justification	
By <i>lt</i>	
Distribution/	
Availability Codes	
Dist	Avail and/or Special
A1	



## INTRODUCTION

Our research goal is to determine the parameters that lead to intrinsic and extrinsic failure of ceramic capacitors. To achieve this goal, we are making electrical measurements and microstructural evaluations on both commercial and laboratory prepared specimens with the following test methods: 1) destructive microstructural evaluation, 2) I-V measurements in both low voltage and degradation field regions, and 3) thermally stimulated polarization and depolarization current measurements. ←

Our preparation and test procedures are based on experience gained from previous programs at Linden Laboratories, Sprague Electric Company, Pennsylvania State University (PSU), and University of Missouri-Rolla (UMR). Because the details of the techniques were given in our original proposal, they will not be repeated here.

## CURRENT STATUS, ACHIEVEMENTS, AND FUTURE STUDIES

### Current Status

The program is nearly on schedule, and most of our goals have been met.

### Achievements

The most notable achievements have been:

- a) developing the computer interfaced I-V system, which allows us to measure resistances as high as  $10^{10}$  ohms at room temperature on 90 specimens under nine to ten different conditions;
- b) setting up a TSC system, which can be used routinely on a wide variety of capacitor specimens;
- c) completing the powder synthesis and fabrication of most of our test specimens;
- d) setting up a test program with industry and Draper that allows us to sample a large number and variety of commercial units. This program involves an evaluation of the ability of the methanol and 85/85/1.5 volt tests to act as effective screens.

- e) establishing a working arrangement with PSU that will make it possible for both our programs to benefit from one another. This will involve the sharing of specimens and coordinating research activities.

The objectives that have not yet been achieved are as follows:

- a) We have not established whether the TSC technique will give us definitive information with regard to capacitor reliability. We do see differences in spectra between various capacitor formulations and can distinguish X7R from Z5U and NPO. In addition, we can see differences related to cation stoichiometry and between units with low and high leakage current. However, we still cannot say for certain that it is an effective test method. We anticipated that the answers would be evident by now, but this is not the case. Progress is being made, but "the jury is still out".
- b) We have not found a unit that displays the classic low voltage failure. Testing is continuing on units that fail the methanol screen, but no results can be reported yet. Dr. Ewell (*formerly from Hughes*) recently provided us with some units that showed low voltage failure in a recent NASA study, but we have not tested them. These units will be tested before the September Electronics meeting in New York.

#### **Future Studies**

Over the next year, we will continue the low voltage, degradation and TSC studies on both commercial and laboratory units. The influence of cation stoichiometry and dopants will be featured.

We will present three to five papers. Two papers will be published, and an MS thesis will be prepared. The sharing of data and specimens with PSU will be expanded, and the interaction between graduate study programs expanded. During this period, the value of the TSC technique for reliability studies should be firmly established.

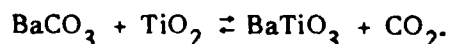
## CURRENT PROGRAM

### Specimen Preparation and Compositions

#### Preparation

**Chemical Preparation.** - Our method of preparing the barium and strontium titanates was first described by Pechini.<sup>1</sup> Essentially, the process, termed the "liquid-mix" process, involves the quantitative mixing and dissolution of the desired cations into a citric acid, ethylene glycol solution. This solution is evaporated into an amorphous polymer, and subsequent calcination yields the desired compound (Fig. 1).

Powders prepared in this manner have several advantages over those prepared by other chemical preparation methods. Conventionally, barium titanate is formed by the solid state reaction



Unfortunately, because this process is diffusion-controlled and will never go to completion, it results in a chemically-inhomogeneous powder. In the liquid mix process, no precipitation occurs, therefore, the cations are randomly distributed throughout the solution. Upon solidification, a glassy resin forms with the cations being linked to the oxygen radicals of the organic network. Calcination of this solid at temperatures below 700°C yields chemically homogeneous uniform crystallites of approximately 500Å particle size. No mechanical grinding, which introduces impurities, is needed to prepare the powder for pressing and subsequent formation of sintered dense compacts. With careful experimental work, the only impurities present in compounds prepared in this manner come from the raw materials themselves.

In addition, when doping is desired, the liquid mix process randomly distributes the dopant cations and produces a homogeneous mixture. Normally, dopants are mechanically added as their oxides, and one relies upon solid state diffusion to distribute the dopant into the grains. This results in a concentration of the dopant across the grains, and this is unsuitable for our purposes.

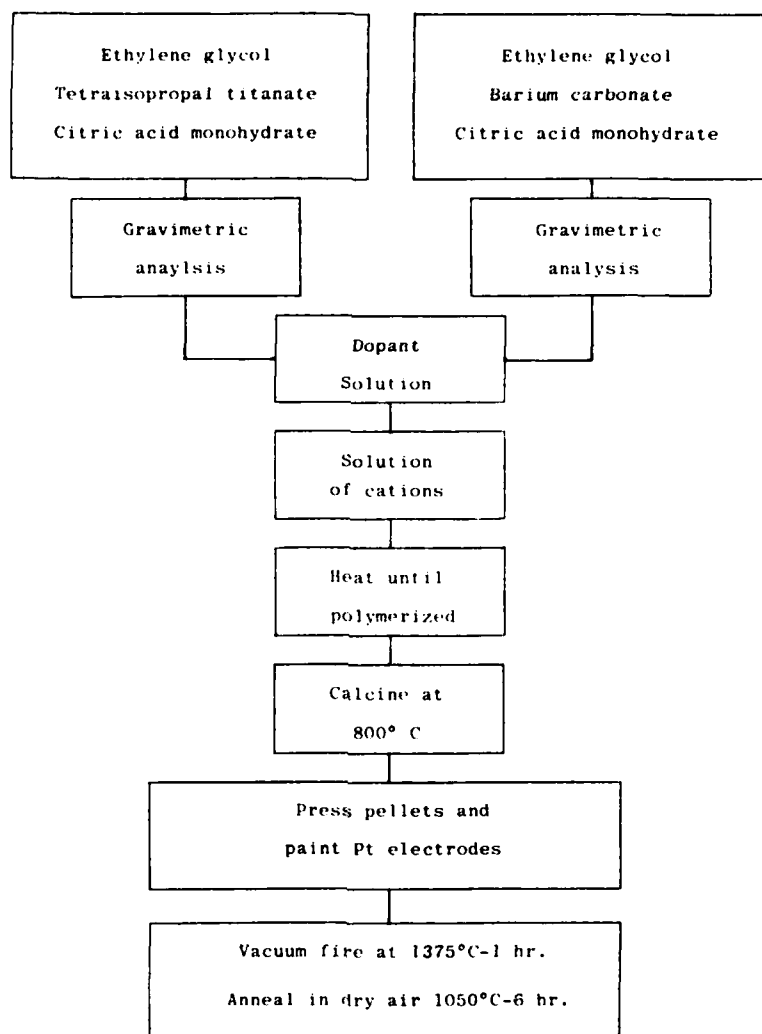


Figure 1. Typical Flow Sheet for Preparation of BaTiO<sub>3</sub> Capacitors.



Other chemical preparation methods described by Kiss et al.<sup>2</sup> and Mazdiyasni et al.<sup>3</sup> depend upon hydrolysis-pyrolysis techniques. Marcilly et al.<sup>4</sup> remarked that these techniques are restricted by the stoichiometric requirements of complex salts and the inhomogeneity of the liquid medium during precipitation. Their study supports the view that the liquid mix process is superior to normal solid state, diffusion-controlled methods.

Basically, then, the liquid mix process is an advantageous method of preparing the powders needed for our study. Not only does it yield chemically homogeneous crystallites, but their small, uniform particle size makes it unnecessary for further processing before fabrication. In addition, we are assured that the dopants being studied will be uniformly distributed throughout the compound.

The experimental procedure used to prepare the compounds is as follows:

- a) Initially a  $\text{Ti}^{+4}$  source is prepared by adding 200 ml of tetraisopropyl titanate (TPT) to 600 ml of ethylene glycol and 400 grams of anhydrous citric acid. This solution is heated on a hot plate at approximately  $120^{\circ}\text{C}$  to dissolve the citric acid and the white, hydrated  $\text{TiO}_2$ , which forms upon initial mixing.

The concentration of  $\text{Ti}^{+4}$  in this organic solution is determined gravimetrically by carefully evaporating the solution in a crucible until a polymer forms. This polymer is then slowly calcined in a furnace until  $800^{\circ}\text{C}$  is reached, held for at least eight hours, and then cooled to room temperature. Only  $\text{TiO}_2$  is left. Careful weight measurements during this process yields the concentration in moles of  $\text{Ti}^{+4}$  per gram solution.

- b) The  $\text{BaCO}_3$ ,  $\text{SrCO}_3$ ,  $\text{MgCO}_3$ ,  $\text{La}_2(\text{CO}_3)_3 \cdot x\text{H}_2\text{O}$ ,  $\text{Al}(\text{NO}_3)_3 \cdot x\text{H}_2\text{O}$ , and  $\text{PbCO}_3$  are all gravimetrically standardized for their respective cation concentrations through calcination in a furnace. All the carbonates or nitrates are driven off, leaving the pure oxides. The resulting oxides are X-rayed

to ensure completion of the reaction and the purity of the end product. Because these cations dissolve readily as salts (in the organic  $Ti^{+4}$  solution), it is not necessary to predissolve them.

- c) Niobium oxalate serves as the  $Nb^{+5}$  source. It is dissolved in hot distilled water and then gravimetrically analyzed for Nb content. Zirconium acetate serves as the  $Zr^{+4}$  source in exactly the same manner. Prior dissolution of these cations is necessary because of the precipitation problems experienced when the solid acetate or oxalate is added directly to the  $Ti^{+4}$  solution.

A complete list of raw materials and sources is included in Table I.

**Table I**  
**Raw Materials and Sources**

<u>Material</u>	<u>Source</u>
$BaCO_3$	E. I. DuPont, De Nemours & Co., Solid State Dielectrics Division
$SrCO_3$	E. I. DuPont, De Nemours & Co., Solid State Dielectrics Division
Tyzor TPT (Tetraisopropyl Titanate)	E. I. DuPont, De Nemours & Co., Chemicals Division
Ethylene Glycol	E. I. DuPont, De Nemours & Co., Chemicals Division
Anhydrous Citric Acid	Chem Tech Industries
$Al(NO_3)_3 \cdot xH_2O$	Apache Chemicals
$La_2(CO_3)_3 \cdot xH_2O$	Apache Chemicals
Niobium Oxalate	Fisher Scientific
Zirconium Acetate	Fisher Scientific
$Mg(NO_3)_2$	Fisher Scientific
$PbCO_3$	Fisher Scientific

Barium titanate or strontium titanate of any cation stoichiometry can be prepared from the raw materials mentioned above by adding predetermined amounts of barium or strontium carbonate to the correct amount of  $Ti^{+4}$  solution. For the doped cases, the A/B ratio is fixed equal to one, with the appropriate adjustments being made depending on which site the dopant is substituted.

Initially, the required raw materials are weighed and placed in a beaker and heated on a hot plate at approximately 90°C. This allows the cations bound as carbonates (or nitrates) to go into solution. This liberates either  $CO_2$  or NO gas. This is the most important step in the process, because complete dissolution of the cations is absolutely necessary. The resulting clear solution is evaporated until an amorphous, organic polymer forms. This solid is heated to 400°C in the beaker to decompose the organics. This results in a black chunky mass. After it is transferred to a crucible, the solid is calcined at 700°C for at least eight hours. X-ray diffraction analysis is used to confirm the compound formation.

**Pressing.** - Before the powders are pressed into discs, 6 w% of a 12 w% water/polyvinyl alcohol solution (PVA) is added as a binder. Thorough mixing is accomplished by shaking the powder and binder in a plastic vial with plastic balls. This procedure crushes many of the agglomerates that form during the final calcination step.

The powder is pressed into pellets approximately 1mm thick in a 1.25 cm diameter stainless steel die at a compaction pressure of  $3500 \text{ kg/cm}^2$  (50,000 psi). Previously, Keck<sup>5</sup> had had a problem when his pellets would rupture after the die was released. He solved this by using a vacuum die. Our PVA binder system, however, seems to have removed this rupture problem. Initially, ten pellets of each composition are pressed.

**Firing.** - The pellets are fired in an electric tube furnace at 1250°, 1300°, 1350°, and 1400°C with a soak time of four hours. Variation of the firing temperature allows us to study the effects of porosity and grain size on the properties

measured, namely degradation. The pellets are fired in air in an alumina muffle tube on a zirconia setter covered with either pure barium titanate or strontium titanate powder. Each series of compositions, barium or strontium titanates, has its own alumina tube for firing. These steps have been taken in order to minimize the introduction of impurities during the firing process.

**Metallization.** - By using a circular stencil, the pellets are metallized with unfritted platinum paste. The electrodes on each pellet do not extend to the edge so that the surface conduction path is approximately four times longer than the thickness. The paste is dried for 30 minutes at 100°C. The pellets are then fired at 800°C for two hours. The furnace is heated and cooled slowly to minimize thermal shock or microcracking. To date, no adhesion problems have been encountered.

### **Compositions**

#### **Nonstoichiometric Ba<sub>x</sub>TiO<sub>3</sub>**

A/B = 0.96, 0.97, 0.98, 0.99, 0.995, 0.998, 1.000, 1.002, 1.005, 1.01, 1.02, 1.03, 1.04.

We selected thirteen nonstoichiometric barium titanate compositions in order to determine the effects of excess barium or titanium on the degradation. We are also interested in the effects of the grain size, porosity, and density of the titanium or barium-rich phases. We chose small variations near A/B = 1 to determine precisely through microstructural examination where the stoichiometry is located.

#### **Donor-Doped BaTiO<sub>3</sub>**

$\text{Ba}_{1-x}\text{La}_x\text{TiO}_3$   $x = 0.001, 0.005, 0.01, 0.05$

$\text{BaTi}_{1-x}\text{Nb}_x\text{O}_3$   $x = 0.001, 0.005, 0.01, 0.05$

We used eight donor-doped barium titanates, with donors chosen to occupy both the A and B sites, in order to study the effect on degradation.

### Acceptor-Doped BaTiO<sub>3</sub>



We used eight acceptor-doped barium titanates to study their effect on degradation. Note, both two and three valent cations are substituted onto the B site.

### Shifted BaTiO<sub>3</sub>



We doped 15 barium titanate compositions with cations that would shift the Curie point. Lead cations are the only ones that will move the Curie point to a higher temperature. We will study the effects of these shifters on degradation.

All of the above compositions, with the exception of the shifted barium titanates, were also chosen for strontium titanate, and we have formulated a total of 73 compositions.

## Compound Preparation and Fabrication

### Compound Preparation

To date, we have used the liquid-mix process to prepare 25 gram batches of all 73 compounds. Thus, this stage of the procedure is complete, and all the batches have been shaker milled to break up the agglomerates that form during the calcination stage. We have also X-rayed them with an XRD-700 diffractometer to ascertain their purity and homogeneity.

### Pressing

For each composition, we need to press ten pellets as described earlier. We fire two pellets of each compound at each of the four firing temperatures so that two green pellets are held in reserve in case of breakage. Currently, we have pressed about two-thirds of the required 730 pellets. We will continue pressing

on a daily basis and expect to be finished soon. We have not had any problems with rupturing or laminations.

### **Firing**

Currently, we have fired 200 pellets of the 730. The firing stage is lagging at the moment because of the limited space in our furnace. Only four pellets can be fired at a time. Just recently, we put another SiC furnace into operation, and this should facilitate the firing of the remaining pellets. Thus far, we have encountered no problems, and we are making firing runs on a daily basis.

### **Metallization**

Currently, we have equipped only 30 pellets with electrodes. We will metallize the remaining pellets as soon as we have completed the structural measurements, which include theoretical density, porosity, grain size, and microstructure. Our preliminary results indicate that the problem of the adhesion of the platinum to the fired surfaces of the pellets is negligible.

In summary, we have prepared all of the compounds to be analyzed in the study. We have pressed most of them into pellets and are currently firing the pellets. This portion of the program should be completed in the next two to three months.

### **Measurements**

Before we metallize the pellets, we need to determine their density, porosity, and grain size. To do this, we are using a Zeiss Axiomat Metallograph to analyze the microstructure of the fired surface of each pellet. We are using the ASTM C-20 74 test, with M-Xylene as the saturating liquid, to determine the densities and porosities. Figures 2 through 17 display the microstructures of some of the pellets. The effects of excess titanium are easily seen in Figures 2 through 11. In these figures, a duplex structure can be seen because of the exaggerated grain growth that occurs from liquid formation in the excess titanium region. As the Ba/Ti

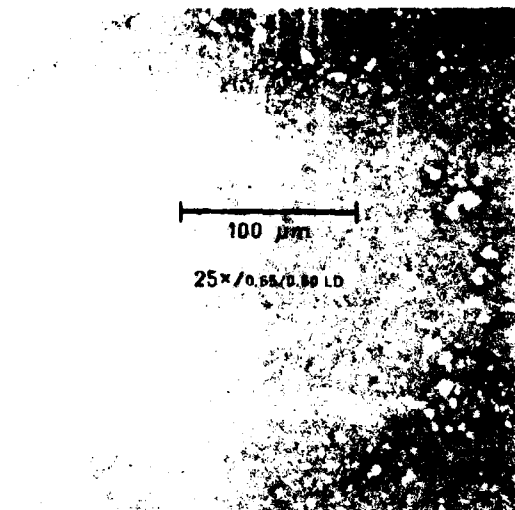


Figure 2. Optical photomicrograph of Ba<sub>0.96</sub>TiO<sub>3</sub> sintered at 1300°C, 4 hr.

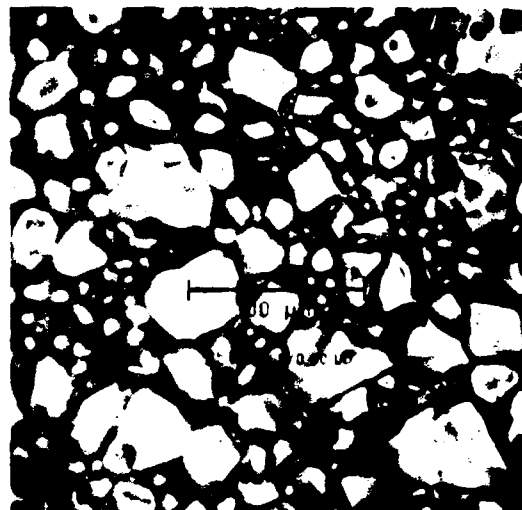


Figure 3. Optical photomicrograph of Ba<sub>0.96</sub>TiO<sub>3</sub> sintered at 1400°C, 4 hr.

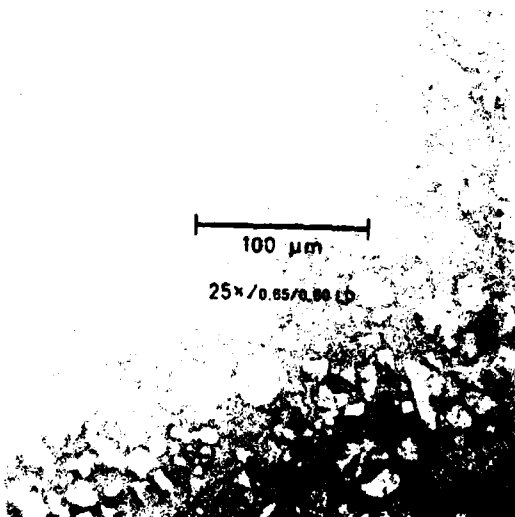


Figure 4. Optical photomicrograph of Ba<sub>0.97</sub>TiO<sub>3</sub> sintered at 1300°C, 4 hr.

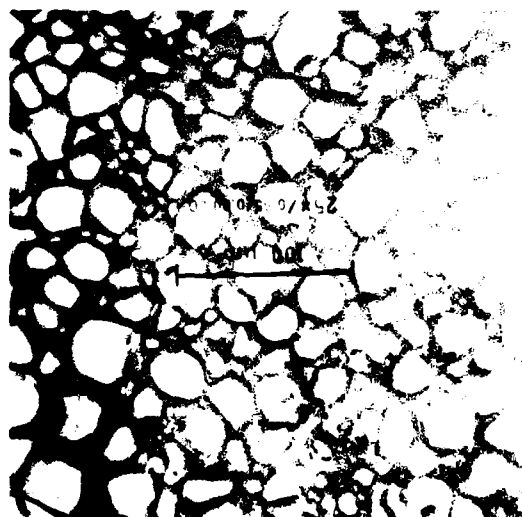


Figure 5. Optical photomicrograph of Ba<sub>0.97</sub>TiO<sub>3</sub> sintered at 1400°C, 4 hr.

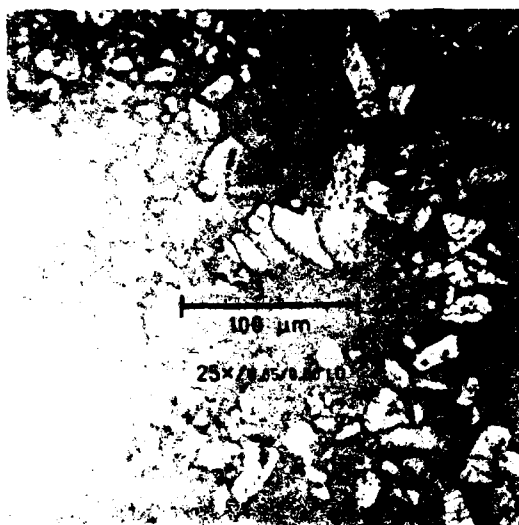


Figure 6. Optical photomicrograph of  $\text{Ba}_{.98}\text{TiO}_3$  sintered at  $1300^\circ\text{C}$ , 4 hr.

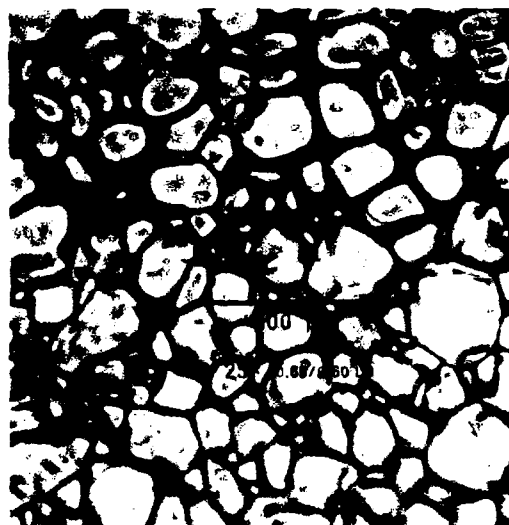


Figure 7. Optical photomicrograph of  $\text{Ba}_{.98}\text{TiO}_3$  sintered at  $1400^\circ\text{C}$ , 4 hr.



Figure 8. Optical photomicrograph of  $\text{Ba}_{.99}\text{TiO}_3$  sintered at  $1300^\circ\text{C}$ , 4 hr.



Figure 9. Optical photomicrograph of  $\text{Ba}_{.99}\text{TiO}_3$  sintered at  $1400^\circ\text{C}$ , 4 hr.



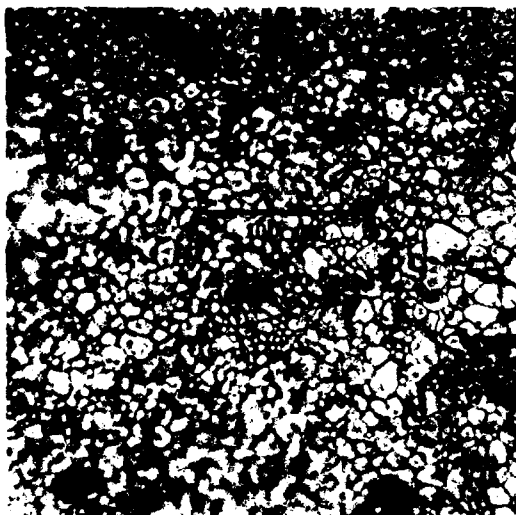


Figure 10. Optical photomicrograph of  $\text{Ba}_{.995}\text{TiO}_3$  sintered at  $1300^\circ\text{C}$ , 4 hr.



Figure 11. Optical photomicrograph of  $\text{Ba}_{.995}\text{TiO}_3$  sintered at  $1400^\circ\text{C}$ , 4 hr.

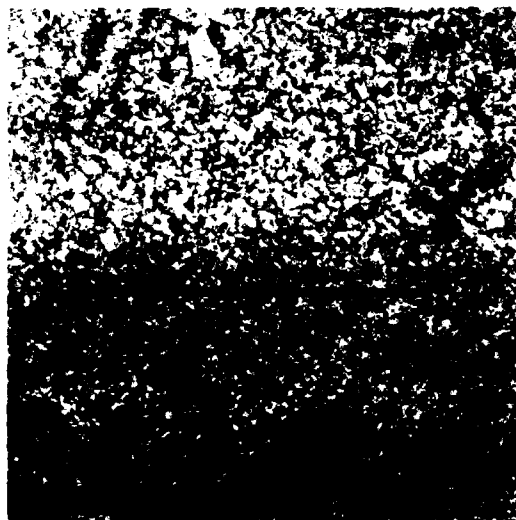


Figure 12. Optical photomicrograph of  $\text{BaTiO}_3$  sintered at  $1300^\circ\text{C}$ , 4 hr.

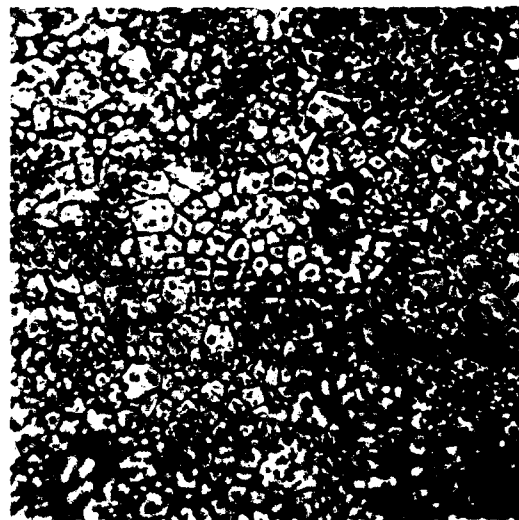


Figure 13. Optical photomicrograph of  $\text{BaTiO}_3$  sintered at  $1400^\circ\text{C}$ , 4 hr.



Figure 14. Optical photomicrograph of Ba<sub>1.002</sub>TiO<sub>3</sub> sintered at 1300°C, 4 hr.



Figure 15. Optical photomicrograph of Ba<sub>1.002</sub>TiO<sub>3</sub> sintered at 1400°C, 4 hr.

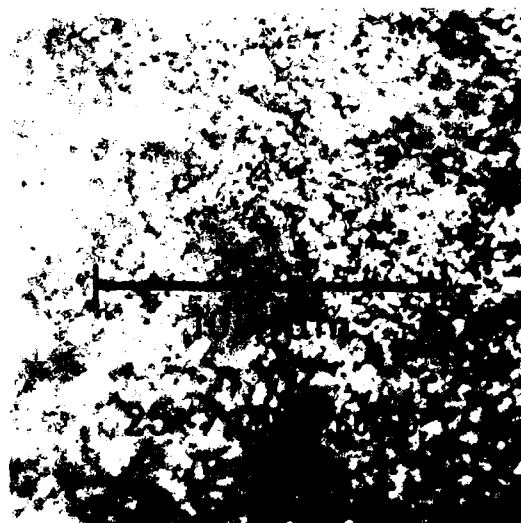


Figure 16. Optical photomicrograph of Ba<sub>1.01</sub>TiO<sub>3</sub> sintered at 1300°C, 4 hr.

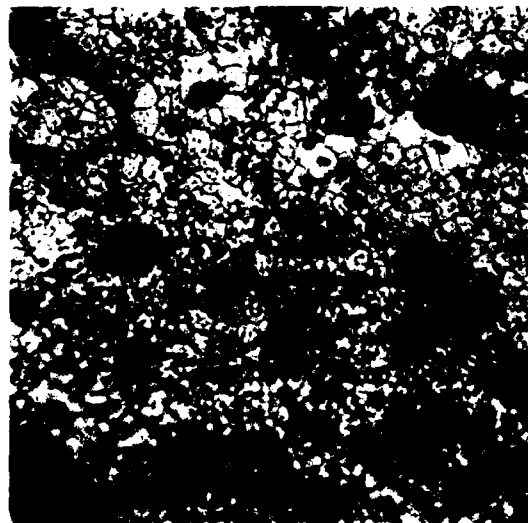


Figure 17. Optical photomicrograph of Ba<sub>1.01</sub>TiO<sub>3</sub> sintered at 1400°C, 4 hr.

ratio approaches 1.000, the amount of liquid decreases until in the  $A/B \approx 0.995$  to 1.000 region normal grain growth occurs (Figs. 10-13). When  $Ba/Ti$  exceeds 1.000, growth is inhibited because of the formation of  $Ba_2TiO_4$  (Figs. 14-17). Table II contains the density, porosity, and percentage of theoretical density of these compositions.

**Table II**  
**Densities and Porosities of  $Ba_xTiO_3$  Formulations**

Compound	Firing Temp. (°C)	Open Porosity (%)	Bulk ( $g/cm^3$ ) Density	% Theoretical Density*
$Ba_{.96}TiO_3$	1300	13.5	5.06	84.3
	1400	2.4	5.29	88.1
$Ba_{.97}TiO_3$	1300	4.0	5.48	91.3
	1400	3.91	5.35	89.3
$Ba_{.98}TiO_3$	1300	3.25	5.58	93.0
	1400	2.16	5.51	91.9
$Ba_{.99}TiO_3$	1300	.57	5.79	96.5
	1400	.13	5.72	95.4
$Ba_{.995}TiO_3$	1300	8.25	5.31	88.4
	1400	5.64	5.25	87.5
$BaTiO_3$	1300	1.77	5.64	94.0
	1400	.11	5.66	94.4
$Ba_{1.002}TiO_2$	1300	8.56	5.38	89.7
	1400	6.13	5.39	89.9
$Ba_{1.01}TiO_3$	1300	3.30	5.59	93.2
	1400	2.24	5.62	93.7

\* The density of  $BaTiO_3$  is  $6 g/cm^3$ .

These figures essentially show that cation stoichiometry occurs at  $A/B \approx 0.995$  and that variations on either side show evidence of the influence of either excess barium or titanium. This means that our original formulations were slightly deficient

in barium. This is generally the case, because  $\text{BaCO}_3$  is always slightly hydrolyzed so that less barium is added than the chemical formula indicates. Thus, we will adjust future compositions to reflect this deficiency.

After the microstructure of the pellets has been analyzed and the pellets metallized, we will be ready to run our tests. The first test is the TSPC-TSDC experiment, which is described elsewhere. Currently, we have made only the  $\text{Ba}_x\text{TiO}_3$  formulations. Keep in mind, however, that the majority of the electrical measurements we have already made have been on commercial units. After we run the TSPC-TSDC measurements, we will analyze each composition for its current vs. time (I vs. t) current vs. applied field (I vs. E), and capacitance vs. temperature (C vs. T) behavior. Currently, we have not measured any laboratory prepared capacitors but intend to do so within the next several months.

#### **Low Voltage Electrical Measurements**

Most of the period covered by this report has been devoted to the construction of the computer-controlled capacitor life-testing equipment. The heart of the system is a Hewlett Packard (HP) 3054 DL Data Logger, which consists of a HP 85 computer integrated with a HP 3497A Data Acquisition Control Unit (Fig. 18). This unit monitors the leakage current of up to 90 capacitors, which are housed in a stack of nine furnaces (Fig. 19). Each component of the system is described below.

**Hewlett Packard 3054 DL Data Logger.** - As stated above, this unit consists of the HP 85 computer and the HP 3497 voltmeter. The computer has a 32K random access memory (RAM) with a built-in thermal printer and tape drive. Data collected with the system are stored on tape and can be recalled for printing, plotting, or statistical analysis. The HP 85 is connected to the HP 3497A through a HP1B interface. The HP 3497A is a 100-channel autoranging voltmeter with  $1\mu\text{V}$  sensitivity. The 100 channels consist of four 20-channel relay multiplexor assemblies with Hi, LO, and guard terminals as well as a 20-channel relay multiplexor with



Figure 18. Photo of Hewlett  
Packard 3054 DL Data  
Logging System.

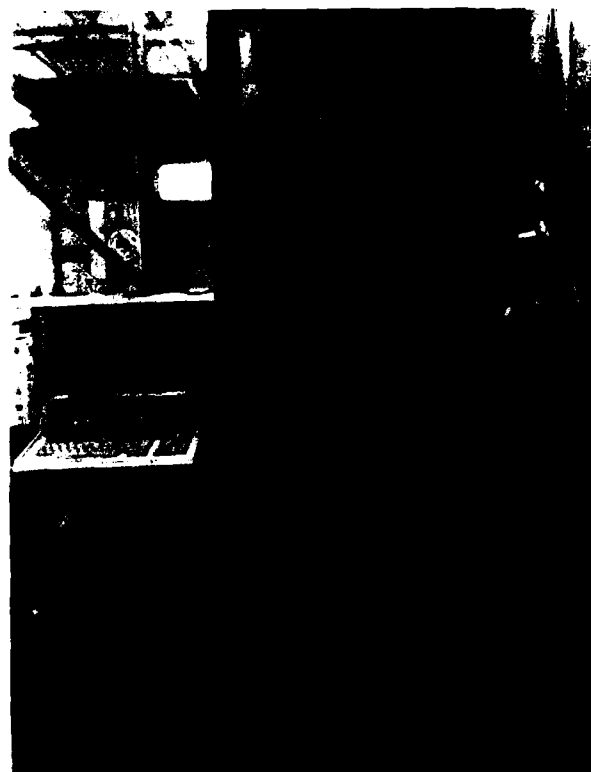
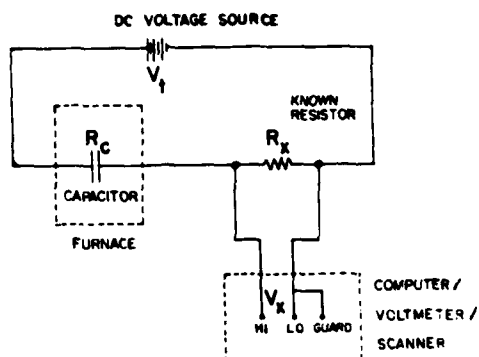


Figure 19. Photo of Com-  
plete Capacitor Life-  
Testing Apparatus.

thermocouple compensation. The latter contains an isothermal reference junction for accurate temperature readings. Each channel is connected to a capacitor to be tested with the circuit shown in Figure 20. The information collected by the HP 85 through the HP 3497 is the voltage drop across the known resistor. The DC voltage supply is a Harrison Laboratories Model 8028 Twin Low Voltage Power Supply, variable from 0 to 40 DCV.



$$\text{VOLTAGE READ : } V_x = V_t \left[ \frac{R_x}{R_c + R_x} \right]$$

$$\text{CAPACITOR'S RESISTANCE : } R_c = \left[ \frac{V_t R_x}{V_x} \right] - R_x$$

$$\text{LEAKAGE CURRENT : } I_c = \left[ \frac{V_x}{R_x} \right]$$

Figure 20. Schematic Circuit Diagram for Low Voltage Capacitor Leakage Current Measurement System.

**Furnaces.** - Each furnace consists of a copper inner shell with a heavy copper faceplate, which is wrapped with heat tape and surrounded by one inch of fiber insulation. This is all housed in an aluminum box. We used copper as the furnace material to ensure an even temperature distribution. We mounted nine furnaces vertically in a cabinet, which contains all of the necessary electrical and atmospheric connections.

All of the furnaces have individual temperature and atmosphere control capabilities (Fig. 21). An Omega 6100 temperature controller with a variable autotransformer is capable of varying the furnace temperature up to 300°C. The temperature controller/furnace combination is capable of maintaining the desired temperature  $\pm 0.7^\circ\text{C}$  over an indefinite period. The atmosphere control desired for our study mainly consists of varying the percentage of relative humidity in each furnace. This is accomplished by passing the furnace air through water, which is heated in an Erlenmeyer flask wrapped with heat tape (Fig. 22). The humidity can be varied by varying flow rates and water temperature. Water temperatures are monitored with an Omega Model 199 temperature meter. In case a different atmosphere is desired, bypass valves allow total avoidance of the water injection system.

Electrical Connections to Capacitors. - Capacitors to be tested in the life-testing apparatus are connected to the computer by mounting them on a printed circuit board capable of withstanding 180°C (Fig. 23). This board is connected to a connector mounted on the copper faceplate, which in turn is wired to the computer (Fig. 24). The wiring is composed of a 22-conductor shielded cable. Each card holds 10 capacitors, but they may be expanded to 24 if additional channels for the data logger become available. Each card has a thermocouple mounted next to the capacitors.

Summary. - The entire life-testing apparatus, except for the humidity control, has been assembled and operated for five months. The atmosphere control has been installed and has been functioning for the past three months. Initially, extensive noise at the 10-12 amp level was encountered as a result of grounding problems; however, proper earth grounding of all wiring and the furnaces themselves has minimized this difficulty. The system is sensitive enough to detect the small changes in resistance of the monitored capacitors because of temperature variations in the



Figure 21. Individual Furnace with Temperature Controller, Flow Meter, and Circuit Board That are Used in Capacitor Life Test System.

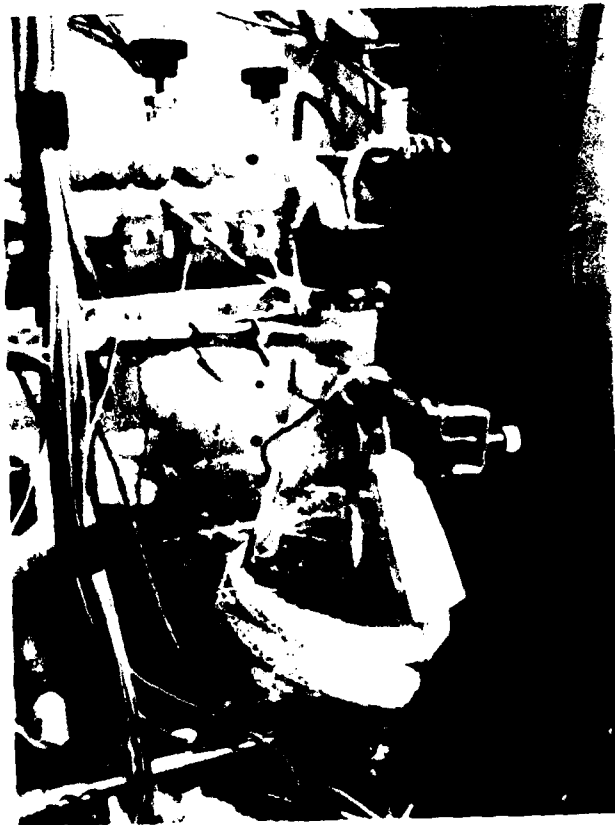


Figure 22. Heated Erlenmeyer Flask Used for Humidity-Control Portion of the Capacitor Life Testing System.



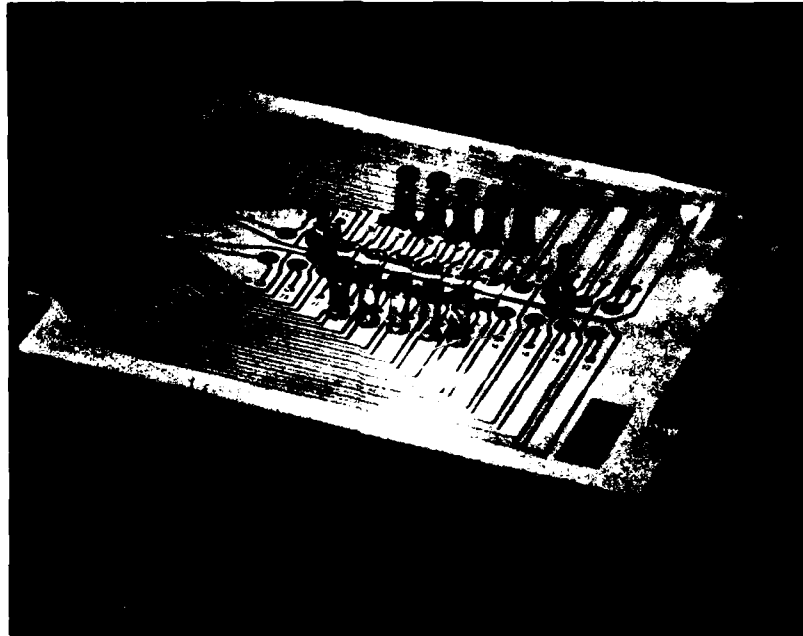


Figure 23. Circuit Board Used for Mounting Capacitors to be Tested in Capacitor Life Test System.



Figure 24. Wiring Connections Made to Individual Furnace, Which is Employed in Capacitor Life Test System.

furnaces of  $\pm 1^\circ\text{C}$ . Because the purpose of the apparatus is to detect the failure of parts characterized by resistance drops of several orders of magnitude, these variations are considered negligible, and we believe the system is capable of detecting changes in resistance as small as one-fiftieth of an order of magnitude.

To date, all of the capacitors, which we have tested, have been commercial units supplied to us by vendors who support their reliability towards low-voltage degradation. We are testing both the BX and NPO formulations. Test conditions are the standard  $85^\circ\text{C}/85\%$  relative humidity with a 1.5 DCV bias. These capacitors have remained at these conditions for nearly 2000 hours. We have used the initial group of capacitors primarily to test the system for sensitivity, temperature stability, and efficiency of the computer program.

At the moment, the program we are using to monitor the capacitors is one that came with the computer. This program measures the leakage current of the tested parts and their temperature once every 30 minutes. There is a problem, however, in storing this huge amount of data on tape. A program we are currently developing will keep track of a running average of the leakage current of each capacitor and record this average on tape only if it differs from the last recorded value by 5%. This will eliminate unnecessary data and save space on the data storage tapes.

In summary, we have designed and constructed a computer-controlled data logging system for life-testing capacitors that is very sensitive and easily capable of acquiring the needed information. Table III illustrates some typical results. To date, we have monitored with excellent results nearly 90 capacitors for almost 2000 hours. Unfortunately, none of the capacitors currently in the system appear to be failing drastically, only a few have changed resistance of one magnitude or greater.

**Table III**  
**Temperature Dependence of BX Capacitors**

- Temperature changed from 85 to 92 °C
- Voltage held constant at 5.000 V
- Voltage readings measured across a  $10^7$  ohms resistor in series with the capacitors

CHANNEL #	VOLTAGE @ 85° (V)	RESISTANCE @ 85° (ohms $\times 10^{10}$ )	VOLTAGE @ 92° (V)	RESISTANCE @ 92° (ohms $\times 10^{10}$ )	$V_{85}/V_{92}$
30	.00133	3.76	.00288	1.74	2.17
31	.00118	4.24	.00252	1.98	2.14
32	.00118	4.24	.00260	1.92	2.20
33	.00122	4.10	.00266	1.88	2.18
34	.00102	4.90	.00213	2.35	2.10
35	.00102	4.90	.00213	2.35	2.10
36	.00073	6.85	.00166	3.01	2.27
37	.00084	5.95	.00174	2.87	2.07
38	.00109	4.58	.00200	2.50	1.83
39	.00071	7.04	.00156	3.21	2.20

Within the next month, we will begin to test units that we have prepared in our laboratory and will also test a wide variety of commercial units. We will debug the new computer program and eliminate most of the gas leakage problems. By being able to test a large, statistically significant number of units, we should be in a position to determine the low-voltage degradation failure mechanism.

#### **High Voltage Degradation**

Over the past several years, we have investigated degradation of ceramic capacitors under DC fields up to 100 volts/mil. Figure 25 is a schematic of the system that was previously used and is now being reassembled. In the new system, up to ten capacitors can be tested simultaneously instead of the previous single sample system.

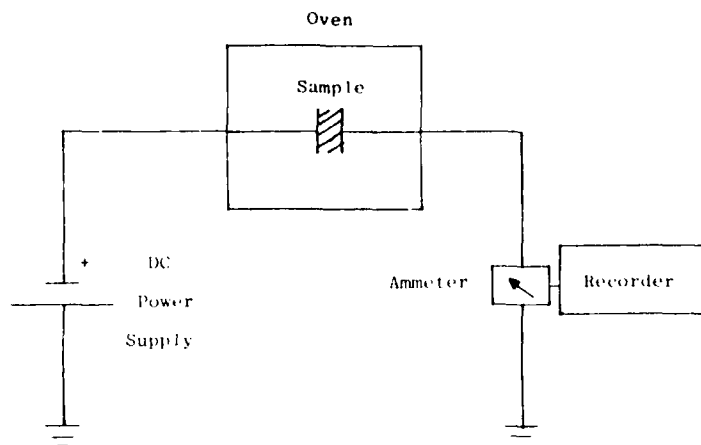


Figure 25. Schematic of the I-V Measurement Apparatus.

Current-voltage-time experiments have been conducted over the temperature range of 80° to 200°C at fields up to 100 volts/mil for times up to 100 hours.

The results can be summarized as follows:

- 1) There exists a strong dependence between degradation behavior and cation stoichiometry. If the ratio  $A/B$  (for  $ABO_3$ ) is  $< 1$ , degradation is rapid with the space charge limited current behavior with an activation energy  $< 1.0$  eV. If the ratio  $A/B \geq 1$ , the dielectrics are stable with ohmic-behavior and an activation energy  $> 1.0$  eV (Fig. 26).
- 2) The influence of doping is related to the dopant type, concentration, and  $A/B$  ratio.

If conditions are established such that the amount of B excess is equal to one-half the amount of donor, oxygen vacancies are eliminated and the greatest stability occurs. Thus, it appears that the key to producing stable  $BaTiO_3$  dielectrics is to adjust the  $A/B$  ratio such that the donors will just compensate the oxygen vacancies. In agreement with the Linden Laboratory reports, all of our evidence points to the fact that the presence of oxygen vacancies is necessary for the degradation process to proceed.

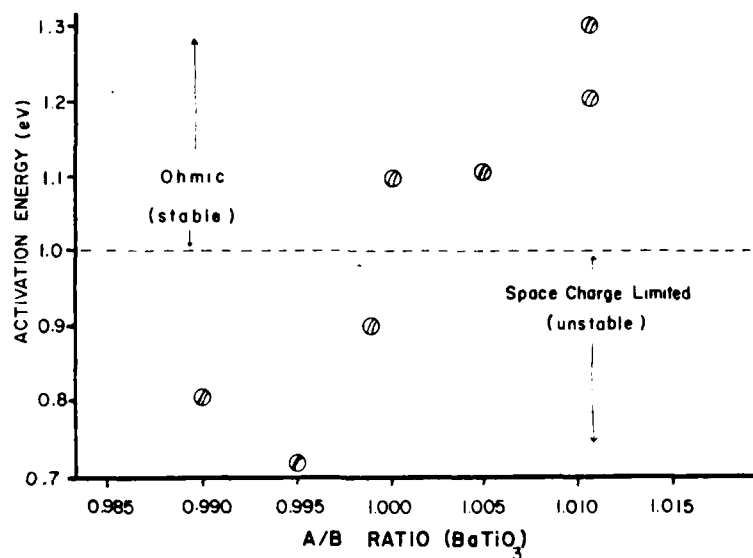


Figure 26. Temperature Dependence of Steady State Leakage Current of  $\text{BaTiO}_3$  as Function of Ba/Ti Ratio.

The influence of acceptors also follows the same pattern with regard to the A/B ratio; however, the fact that the acceptor levels are about 1 eV from the valence band edge, they act as electron traps and tend to stabilize the units toward degradation.

#### Evaluation of Methanol Screen

A nondestructive, low voltage, failure screening technique has been suggested by Chittick et al.<sup>6</sup> In this test the 10VDC leakage current is measured after 10 seconds, the capacitor is preheated to 85°C and immersed in methanol at room temperature for 15 minutes, and the capacitor is rapidly dried in air and remeasured.

Capacitors with flaws that extend to surface show an increase in leakage current after immersion. Researchers at the Standard Telecommunication Laboratories report that this acts as a very effective screen.

It is our intent at this point in our program to use this screening technique to aid us in both our TSPC and I-V measurement studies. Thus, all the dielectrics we

study are being subjected to the methanol screen. It is premature to jump to conclusions, but it does appear that the physically defective units can be detected by this screen if the defect extends to a free surface.

We have not had time to establish a link (if one exists) between this test and our other measurements. We are currently addressing this problem and will discuss it in our next report.

### Injection Mechanisms in Solids

Electronic conduction through an insulator can be separated into three distinct phases: 1) carrier injection from the metal to the insulator, 2) carrier motion through the bulk, and, 3) carrier extraction from the insulator to the metal. Any observed steady-state electrical behavior exhibited by a specific electrode-insulator combination will necessarily be controlled by one of these three phases.

When a metal and an insulator are joined, carriers such as electrons will diffuse from one to the other until their Fermi energies align. If the work function of the metal is less than that of the insulator, electrons will transfer from the metal to the insulator, forming an ohmic contact (Fig. 27). In this case, electrons are able

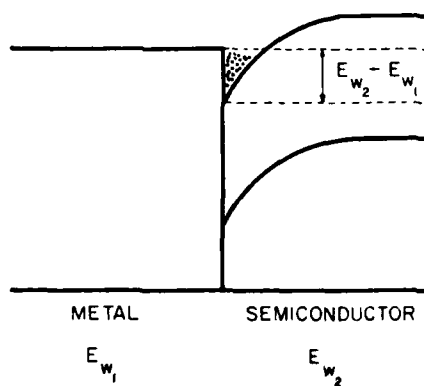


Figure 27. Energy Band Structure at n-Type Semiconduction-Metal for Ohmic Contact.

to move freely in either direction across the interface, not limiting the current in any way whatsoever. Therefore, for thick insulators biased under low fields, with ohmic contacts, observed steady-state behavior is governed by the bulk properties of the insulating medium; the second phase of the conduction process. The simplest example of this phase would be "ohmic" behavior. The governing equation, Ohm's Law, is as follows:

$$J = qn\mu E \quad (1)$$

in which  $J$  is the current density,  $q$  the electronic charge,  $n$  the carrier concentration,  $\mu$  the mobility, and  $E$  the applied field. Note that the bulk properties, such as carrier concentrations and mobility, control the conduction process. From this equation, it can be seen that a  $\log J$  vs.  $\log E$  plot would be linear with slope equal to  $qn\mu$ .

For thinner insulators, biased under higher fields, electrical behavior is not governed by bulk properties but by various current injection mechanisms, which have been identified experimentally. These mechanisms are: Schottky Emission, Tunneling, and Space-Charge-Limited current. Each is discussed separately below.

#### Schottky Emission

The Schottky emission of electrons from a metal to an insulator is analogous to the thermionic emission of electrons from a metal into a vacuum. Essentially, this mechanism involves the escape of electrons from a metal as a result of temperature effects alone.

For a metal-vacuum system, there exists a potential barrier at the surface of the metal that keeps electrons from escaping. The form of this potential barrier is obtained by using the "method of images" approach. This is based on the assumption that an electron leaving the surface induces a positive charge an equal distance into the metal and thereby constitutes an attractive force. The resulting barrier is given by

$$V(X) = \frac{-q^2}{4\pi\epsilon_0 (X^2 + a^2/2)^{3/2}} \quad (2)$$

in which  $V(X)$  is the surface potential barrier,  $q$  the electronic charge,  $\epsilon_0$  the permittivity of free space,  $X$  the distance away from metal, and  $a$  the interatomic spacing of the metal. The form of this barrier is shown in Figure 28. Its height is equal to the work function of the metal.

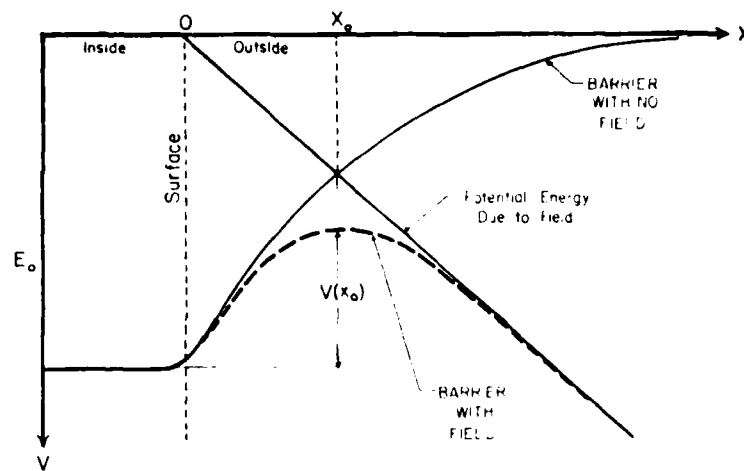


Figure 28. Reduction in the Surface Barrier Due to an External Electric Field.

Only those electrons with sufficient kinetic energy to surmount this potential barrier at the surface of the metal will be emitted. Fermi-Dirac statistics describe the energy distribution of electrons in a metal, i.e., in the velocity distribution of occupied states over those velocities corresponding to energies sufficient to surmount the barrier, a current density relationship may be found. This equation for thermionic emission that is known as the Richardson-Dushman equation is as follows:

$$J = \frac{4\pi m q K^2}{h^3} T^2 \exp - [\phi/KT] \quad (3)$$

in which  $J$  is the current density,  $m$  the electron mass,  $q$  the electronic charge,  $K$  the Boltzman constant,  $h$  the Planck's constant,  $T$  the absolute temperature, and  $\phi$  the surface potential barrier height.



Schottky emission involves the same phenomena as thermionic emission, but an accelerating potential alters the shape of the surface potential barrier thereby increasing the emission. More electrons in the tail end of the Fermi-Dirac distribution have the sufficient "hopping" energy. The surface potential barrier with an applied field is

$$V(X) = \frac{-q^2}{4\pi\epsilon_0 (X^2 + a^2/2)} q E_x . \quad (4)$$

All of the symbols in this equation have been defined, and Figure 28 is its graphic representation.

The effective height of the barrier becomes

$$V(X_0) = -q (q^2/4\pi\epsilon_0)^{1/2} . \quad (5)$$

This potential represents the effective reduction in the work function of the metal as a result of the applied field and makes it easier for electrons to be emitted. After emission, the electrons are removed from the region of the contact and accelerated towards the anode. The equation for Schottky emission then is

$$J = \frac{4\pi m q K^2}{h^3} T^2 \exp \frac{-(\phi - q(q^2/4\pi\epsilon_0)^{1/2})}{KT} . \quad (6)$$

Note that the resulting current density is strongly dependent upon the temperature and the square root of the field. Correspondingly, a plot of  $\log J$  vs.  $E^{1/2}$  (constant temperature), or  $\log J/T^2$  vs.  $1/T$  (constant) would be linear if the Schottky emission were occurring (Fig. 29).

It is also important to note that these equations are derived for a metal-vacuum system. Our interest is in a metal-insulator system whose behavior differs from that predicted for a metal-vacuum only in the magnitude of the surface potential barrier, which results from the difference in work functions between the metal and insulator. The contact necessarily needs to be one that rectifies because the

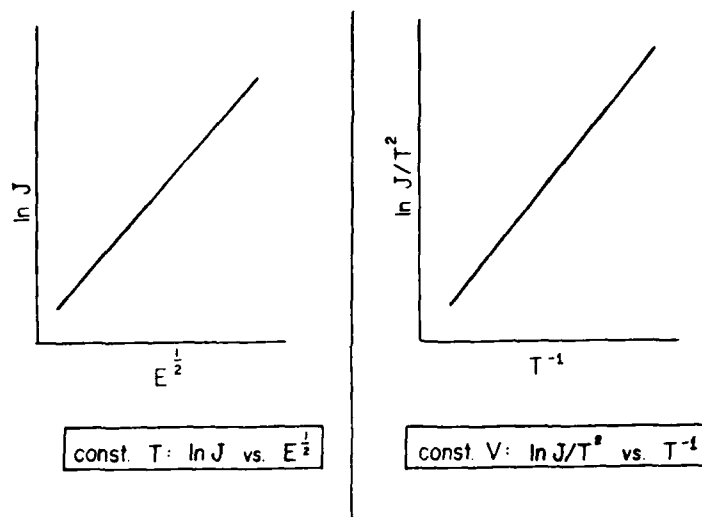


Figure 29. Injected Current as a Function of Electric Field and Temperature Predicted for Schottky Emission.

work function of the metal must be greater than that of the insulator. That or the rectification may be due to a surface depletion layer or a surface dipole layer present at the interface.<sup>7</sup> In any case, electrons that are thermionically emitted from the metal enter directly into the conduction band of the insulator and are swept away towards the anode. This constitutes the Schottky emission current.

The several assumptions or conditions utilized in this approach, which can cause significant deviations from theory, are: 1) Interfacial conditions are ignored. 2) The work function may be temperature dependent. 3) Electrons may be reflected at the surface of the metal. As mentioned previously, charge or dipole layers at the surface may alter the effective work function of the metal-insulator contact. These arise as a result of surface irregularities and interdiffusion of atomic species. The net effect is to change the slope of the  $\log J$  vs.  $E^{\frac{1}{2}}$  graph from expected values, but the observed behavior does not change; Schottky emission still occurs. For semiconducting insulators, the temperature dependence of the Fermi energy alters the surface potential barrier. This has the effect of making the constant voltage,  $\ln J/T^2$  vs.  $1/T$  graph nonlinear; however, this can be accounted for by determining the temperature

dependency of the Fermi energy. Reflection of electrons at the metal surface arises from quantum-mechanical effects, which allow the electrons to be reflected by a potential barrier even though they have sufficient energy to overcome it. A full quantum mechanical treatment of this phenomenon yields a minor effect at extremely high fields and temperatures but produces a more significant effect at lower fields and temperatures where the electrons barely "clear" the barrier.

Schottky emission has been found to occur in insulating materials with thicknesses on the order of 2 mils or less and with applied fields of approximately  $10^5$  V/cm. These conditions correspond to 250 V/mil, which is well within the fields of some multilayer capacitors or of grain boundaries in such devices as barrier layer capacitors and varistors. Several authors have found that Schottky emission occurs in insulating materials:

Emtage and Tantraporn<sup>8</sup> first observed Schottky emission in  $100\text{\AA}$  thick films of polymerized silicon oil with gold electrodes. They concluded that at room temperature the current is totally due to Schottky emission, but at lower temperatures ( $-70^\circ\text{C}$ ), tunneling emission becomes dominant. They also observed Schottky emission in  $50\text{\AA}$  thick  $\text{Al}_2\text{O}_3$  and  $\text{GeO}_2$ .

Lengyel<sup>9</sup> found that 1.1 mil thick films of polyethylene-terephthalate and 2.2 mil thick films of polyvinylformal exhibit Schottky emission as the limiting factor when one tries to establish a steady-state current. The fields vary from 20-200 kV/cm, and temperatures from  $25^\circ$  to  $100^\circ\text{C}$ .

Tantraporn and Harris<sup>10</sup> observed Schottky emission in  $100\text{\AA}$  thick mica.

M. Hacskeylo<sup>11</sup> measured  $100\text{\AA}$  thick films of  $\text{Al}_2\text{O}_3$  and found that Schottky emission accurately described the current-voltage behavior up to fields as strong as  $10^7$  V/cm.

D. Payne<sup>12</sup> studied 2 mil thick  $\text{BaTiO}_3$  capacitors and found that the current injection mechanism exhibited the current-voltage, current-temperature characteristics described by Schottky emission.

Johansen<sup>13</sup> studied 0.1 to 1 $\mu$  thick films of SiO<sub>2</sub> and observed Schottky emission and the Poole-Frenkel effect. This is internal Schottky emission in which the conduction process is limited by the enhanced thermal emission of electrons from a discrete trap level into the conduction band.

In summary, Schottky emission into insulators is analogous to thermionic emission of electrons from a metal into a vacuum. This current injection mechanism occurs mainly in thin films up to several mils in thickness and under applied fields ranging from 50 to 1000 kV/cm. Of particular interest is Payne's<sup>12</sup> study, which reveals that BaTiO<sub>3</sub> capacitors exhibit non-ohmic behavior, i.e., Schottky emission tends to degrade.

### Tunnel Emission

Tunnel emission, also known as Fowler-Norheim tunneling, occurs in very thin insulators (10-100 $\text{\AA}$ ) under fields on the order of  $10^7$  V/cm. Unlike Schottky emission in which electrons energetically pass over the surface potential barrier of the metal insulator contact, "tunneling" electrons pass through the barrier. This is a quantum-mechanical phenomenon in which electrons are able to pass through an energetically forbidden region. The current density arising from such an injection mechanism is directly proportional to a transmission coefficient, which describes the percentage of electrons that tunnel through the barrier.

For simple "square" barriers, the Schrodinger equation is directly solvable, and an exact transmission coefficient can be found. However, for barriers such as the effective surface potential barrier (Fig. 28), the Schrodinger equation is not solvable, and an approximation method must be used. For tunneling, the Jeffreys-Wentzel-Kramers-Brillouin (JWKB) approximation theory is used. This theory is valid in the region of a slowly varying potential, i.e., the momentum of the electron does not change appreciably over a distance of several deBroglie wavelengths. The transmission coefficient is given by

$$T = \exp \left\{ -2 \int_{x_1}^{x_2} [2m/h^2 (E - V(x))^{1/2} dx] \right\} \quad (7)$$

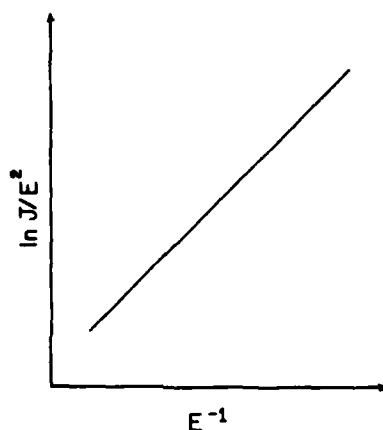
$$= \exp \left[ -4/3 nq \frac{(2m)^{1/2} \phi^{3/2}}{E} \right] \quad (8)$$

in which  $T$  is the transmission coefficient,  $x_1$  the turning point where  $E = V(x)$ ,  $x_2$  the turning point where  $E = V(x)$ ,  $m$  the mass of the electron,  $n$  the Planck's constant/ $2\pi$ ,  $E$  the electron energy,  $V(x)$  the surface potential barrier, and  $\phi$  the work function. If this coefficient is multiplied by the expression for the number of electrons impinging upon the contact per second, one obtains<sup>13</sup>

$$J = \frac{q^3 E^2 \alpha}{8 \pi h \phi} \exp \left[ -4/3 \frac{(2m)^{1/2}}{nq} \frac{\phi^{3/2}}{E} \right] \quad (9)$$

in which  $\alpha$  and  $\beta$  are the adjustable parameters used to fit the data experimentally observed.<sup>14</sup>

A plot of  $\log J/E^2$  vs.  $E^{-1}$  yields a straight line (Fig. 30). The important thing to notice is the temperature independence, which makes it easy to distinguish from Schottky emission.



ln  $J/E^2$  vs.  $E^{-1}$

Figure 30. Injection Current as Function of Field for Tunneling Mechanism.

Tunnel emission in insulators has been identified experimentally by several investigators:

Fisher and Giaever<sup>15</sup> observed that the current injection mechanism in 50Å thick  $\text{Al}_2\text{O}_3$  films is tunneling emission.

Ekrut and Hahn<sup>16</sup> performed extensive studies on tunneling emission in Ta/Ta<sub>2</sub>O<sub>5</sub>/Ag and Al/Al<sub>2</sub>O<sub>3</sub>/Pb junctions. Their oxide thickness was on the order of 10-50Å and was grown by careful oxidation of an electrode.

Maserjian and Zamani<sup>17</sup> studied 50Å thick films of SiO<sub>2</sub> grown on silicon and observed classical Fowler-Nordheim tunneling. An interesting finding of theirs was that the tunnel junction degraded as a function of time, i.e., its current increased. They explained this behavior by introducing the formation of positive-charge centers, which form at the interface.

As stated earlier, tunnel emission occurs only in very thin insulators, which are on the order of several hundred angstroms thick under fields of  $10^7$  V/m. This corresponds to 25,000 V/mil. Obviously, tunneling is not going to occur in multilayer capacitors; however,  $10^7$  V/cm also converts to 10V/100Å, which is not an unreasonable field to see applied across a grain boundary. Matsuoka<sup>18</sup> theorized that ZnO varistors work because the electrons tunnel through a double Schottky barrier at the grain boundary when a critical field is reached. Tunneling is easily identified by its temperature independence and a linear plot when the data are plotted as  $\log J/E^2$  vs.  $E^{-1}$ .

#### Space-Charge-Limited Current

For insulators with ohmic contacts that are biased under high fields, it is possible for electrons to be directly injected into the conduction band of the insulator from the cathode. The injection is at such a rate that all of the electrons cannot immediately move through the conduction band to the anode. This results in a "space charge" buildup at the cathode. This space charge of the uncompensated electrons alters the electric field in such a way as to limit the current, hence, the space-charge-

limited current (SCLC) injection mechanism. This is analogous to the limited emission of electrons through a vacuum from cathode to anode first described by Child<sup>19</sup> in 1911. Child's law is

$$J = \frac{4\epsilon_0}{9} \left(\frac{2q}{m}\right)^{\frac{1}{2}} \frac{V^{3/2}}{X^2} \quad (10)$$

in which  $J$  is the current density,  $\epsilon_0$  the permittivity of free space,  $q$  the electronic charge,  $m$  the electronic mass,  $V$  the applied voltage, and  $X$  the electrode separation.

Mott and Gurney<sup>20</sup> pointed out that a solid state analog of this phenomenon would be possible. Rose<sup>21</sup> later developed this idea into an incisive theory concerning SCLC and its dependence upon intrinsic properties of the insulators themselves.

The main point is this: insulators with ohmic contacts biased under low fields will initially exhibit ohmic behavior, but at some point the field will become high enough such that SCLC behavior will take over. The field at which this will occur depends upon the bulk properties of the insulator, such as free and trapped carrier concentrations and the overall defect chemistry. Different types of SCLC behavior will be exhibited for various combinations of these quantities. Lampert and Mark<sup>22</sup> explicitly derived the various possible cases and their limitations. Basically, there are six cases which can arise: 1) perfect trap-free insulator, 2) trap-free insulator with terminal-free carriers, 3) insulator with shallow traps, 4) insulator with deep traps, 5) insulator with an exponential trap distribution, and 6) insulator with a uniform trap distribution.

The governing current density versus field relationships for each of these cases can be derived by using Poisson's equation and the relationships describing the concentrations of free and trapped carriers as a function of temperature and Fermi energy (Fig. 31). Each case is discussed separately below.

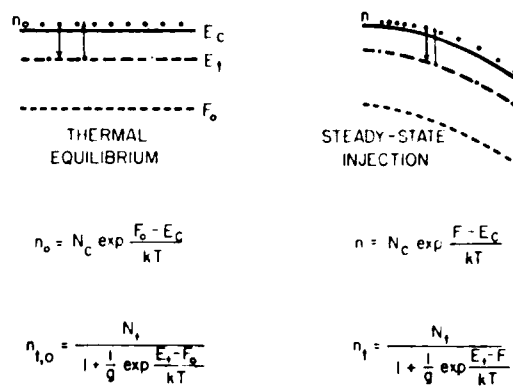


Figure 31. Band Structure at Thermal Equilibrium and for Steady-State Injection for the Space Charge Limited Current Mechanism.

### Perfect Trap Free Insulator

A perfect insulator because of thermal concentration is free of traps and has a negligible concentration of free carriers. This is the simple solid-state analog originally described by Mott and Gurney.<sup>20</sup> All of the injection electrons remain free in the conduction band and contribute to the space charge, which inherently limits the current. The current density is given by

$$J = 9/8 \epsilon \mu \left( \frac{V^2}{L^3} \right) \quad (11)$$

in which  $J$  is the current density,  $\epsilon$  the permittivity of the insulator,  $\mu$  the electron mobility,  $V$  the applied voltage, and  $L$  the electrode separation.

Note the  $J \propto V^2$  dependency -- current increases with the square of the voltage, not linearly as in ohmic behavior. The importance of this simple case is that it represents the highest current that can flow when all the traps are filled, and the injected concentration of electrons is much greater than any other contribution. Thus, the perfect trap-free insulator case is the limiting case for all of the SCLC injection mechanisms at high fields.



### Trap-Free Insulator with Thermal-Free Carriers

This case incorporates the addition of carriers as a result of the thermal ionization of electrons from band to band processes or from donor levels lying close to the conduction band. If one looks at the concentration gradient of electrons across the insulator (Fig. 32) at low fields, the concentration of thermal free carrier numbers is greater than the concentration of the injected carriers, and ohmic behavior is dominant; however, when the concentration of injected carriers exceeds that of thermal free carriers, then the SCLC trap free square law is observed. Graphically, this would appear as a change in slope of magnitude two on a  $\log J$  vs.  $\log E$  plot (Fig. 33). The critical voltage at this transition point is defined as

$$V_c = \frac{8qn_o L^2}{9\epsilon} \quad (12)$$

in which  $V_c$  is the critical applied voltage,  $q$  the electronic charge,  $n_o$  the thermally-ionized free carrier concentration,  $L$  the electrode separation, and  $\epsilon$  the insulator permittivity.

### Insulator with Shallow Traps

If the traps, which are initially empty, exist within the insulator, the net effect will be to decrease the magnitude of the injected current. Electrons, which would have stayed in the conduction band and contributed to the space charge, are captured. For shallow traps (those lying between the conduction band and the Fermi energy) the corresponding current density is reduced by an amount  $\theta$ , which is field independent. Thus,

$$J = 9/8 \theta \epsilon \mu (V^2/L^3) \quad (13)$$

in which  $\theta$  is the ratio of free to trapped carriers.

As before, a transition from ohmic behavior to SCLC will occur as the field increases. The critical voltage now becomes

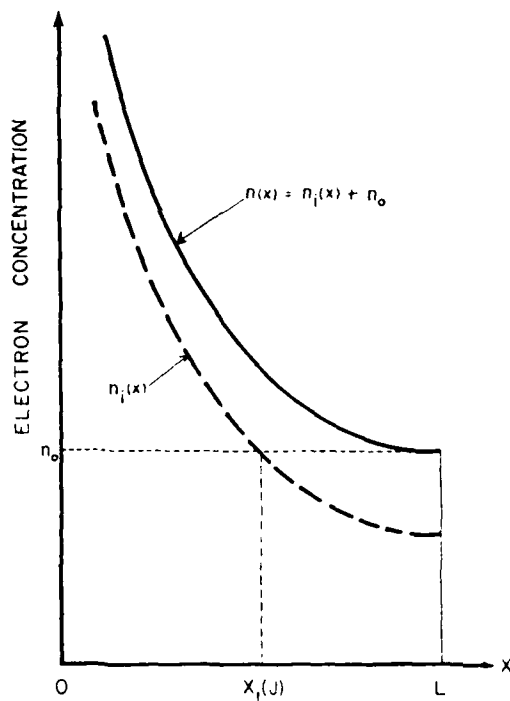


Figure 32. Injected Electron Concentration as Function of Distance from Metal-Insulator Contact.  $n(x)$  is the concentration of injected carriers plus the thermal carriers and  $n_i(x)$  is the concentration of injected electrons.

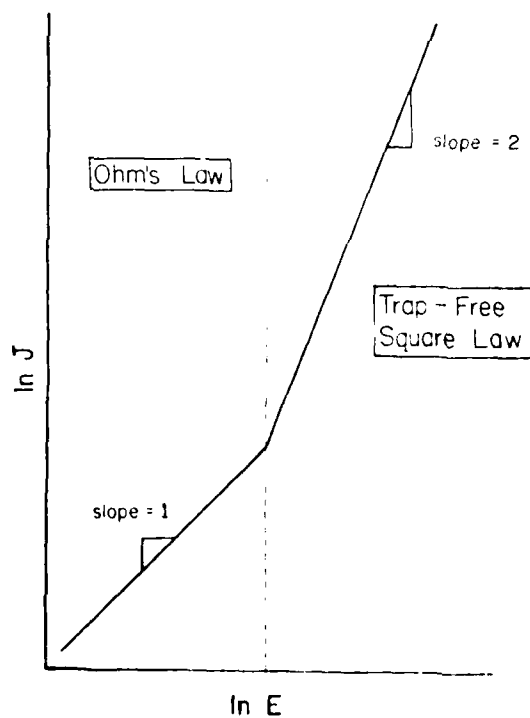


Figure 33. Injected Current for Trap-Free Insulator with Thermal-Free Carriers as Function of Field. This plot illustrates a transition from ohmic behavior to SCLC field when  $n_0 = n_i(x)$  in Fig. 32.

$$V_c = 8/9 \frac{qn_o L^2}{\epsilon \theta} . \quad (14)$$

With an increase in the concentration of traps, the ratio of free to trapped carriers becomes smaller, and the voltage at which the transition occurs increases. This case has been found to be a good approximation for single crystals with high chemical and structural purity. Shallow traps may arise as a result of low lying acceptor states, dislocations, or a myriad of other structural and chemical imperfections.

#### Insulator with Deep Traps

Undoubtedly, some crystals will contain traps that lie energetically between the Fermi energy and the valence Fermi energy and the valence band, i.e., deep traps. In this case,  $\theta$ , the ratio of free to trapped carriers, is no longer field dependent. This is a direct result obtained from Poission's equation and the relationships between the free and trapped carrier concentrations. The result is that at some voltage at which ohmic behavior ceases, there is a region where the current abruptly increases instead of immediately transforming to the trap-free square law. This corresponds to a filling of the discrete, deep traps (Fig. 34).

The significance of this result is extremely important, because if the current-voltage, which was being made on a device, suddenly shot upward, we would naturally assume that a breakdown was occurring and we would shut down the experiment. With the incorporation of SCLC theory, this sudden increase may be otherwise explained. Single crystals of ZnS have been found to exhibit this vertical increase in the current.

#### Insulator with a Uniform Trap Distribution, Insulator with an Exponential Trap Distribution

Real crystals, particularly those of polycrystalline materials, are unlikely to contain a single, discrete trap energy but will most likely exhibit an energetic distribution of traps. This distribution may be uniform or exponential. In any case, the

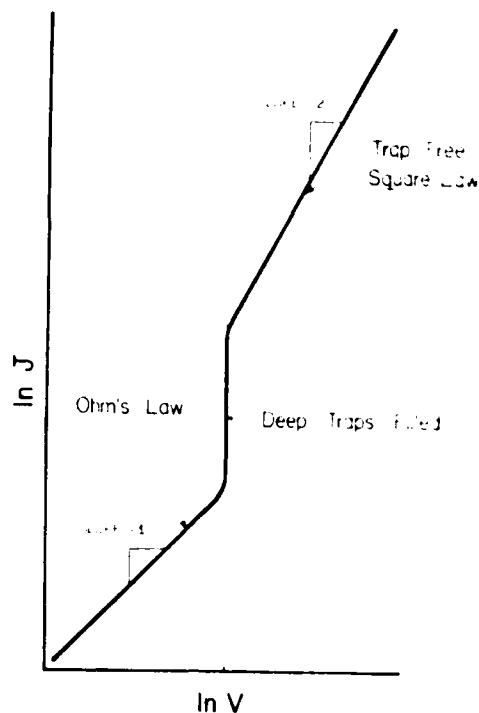


Figure 34. Injected Current as Function of Applied Voltage for Perfect Insulator with Deep Traps.

ratio of free to trapped carriers again becomes field dependent, and in this case results in a more gradual increase in the current after ohmic behavior (Fig. 35). The ratio is exponentially dependent either upon the field or some power law higher than two upon the field.

The most likely exponential distribution of traps would be Gaussian, which represents a "smearing out" of trap energies from a most likely trap energy. In this case, the current density is given by<sup>22</sup>

$$J = q\mu N_c \left( \frac{\epsilon}{qN_o kT_t} \right)^\ell \frac{V^{\ell+1}}{L(2\ell+1)} \quad (15)$$

in which  $N_c$  is the effective density of states in the conduction band,  $T_t$  the characteristic constant of the Gaussian distribution,  $N_o$  the number of traps at the most likely energy of the Gaussian distribution, and  $\ell$  is equal to  $T_t/T$  (the ratio of  $T_t$  to the absolute temperature).

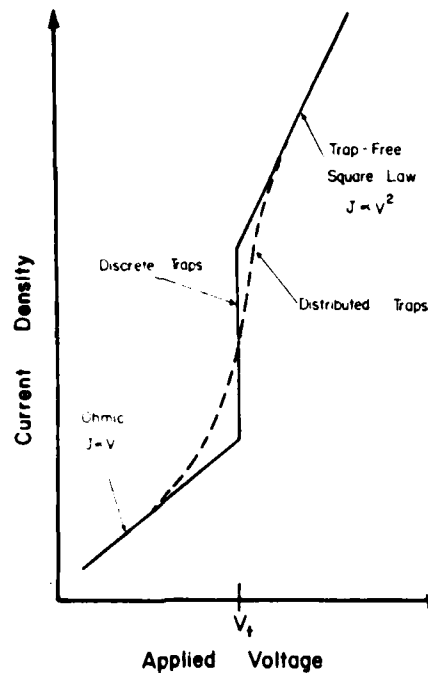


Figure 35. Injected Current as Function of Applied Field for Insulation with Discrete and Distributed Traps.

If the traps are uniformly distributed in energy, the current density-voltage relationship is given by<sup>22</sup>

$$J = q\mu N_0 (V/L) \exp \left( \frac{\alpha V}{2} \right) \quad (16)$$

in which  $\alpha$  is equal to  $\epsilon/qN_n K$ , and  $N_n$  is the trap concentration.

What is happening here, is that at low fields, ohmic behavior is observed as a result of the concentration of thermally-ionized carriers being greater than the concentration of injected carriers. At some critical field, the ratio of free to trapped carriers becomes field dependent because of the distribution of traps. The current increases sharply as these traps fill and contributes to the overall conduction through recombination generation effects. Eventually, a point is reached where the traps are all filled, and again the trap-free square law describes the current density-voltage behavior.

The consequences of this trap-free square law region, which occurs at a high field for all of these cases, are paramount. In this region, the current is limited only by the space charge of the injected electrons. It does not make any difference what is in between the electrodes. This is quite a remarkable result. The existence of an abnormally high leakage current in an insulating device may not be due to problems with the insulator but may be due only to the onset of the SCLC injection mechanism.<sup>7</sup>

The derivation of the preceding SCLC relationships depends upon two key assumptions: 1) the contacts are ohmic but otherwise unimportant and 2) the influence of the contacts on the conduction band profile, i.e., band bending, is confined to a depth that is small compared with the width of the insulator. O'Reilly and DeLucia<sup>24</sup> and Rosenthal and Sapor<sup>25</sup> investigated thin insulators in which the contact regions are significant. Essentially, the conductivity of the insulator increases as a result of the overlap of the space-charge regions of two ohmic contacts. In this case, Rose and Lampert's theory becomes inapplicable. Edwards and Jones<sup>26</sup> addressed themselves to this problem by modeling the zero-bias conduction band profile and investigating its effects on the current density-voltage characteristics.

Space-charge-limited current has been found to occur in insulators several mils thick under applied fields ranging from 1000-10,000 V/cm. This corresponds to only 25 V/mil, not a high field whatsoever. This is well within the range of multilayer capacitors. The question is, does SCLC occur in applicable insulators? The possibility is brought to light by citing some previous experimental work as follows:

Originally, Smith and Rose<sup>27</sup> observed SCLC behavior in CdS single crystals.

Branwood and Tredgold<sup>28</sup> and Branwood et al.<sup>29</sup> measured BaTiO<sub>3</sub> single crystals and found SCLC behavior described by

$$J = a(V/L) + b(V/L)^2 \quad (17)$$

in which a and b are constants used to fit the data. Their single crystals were 100-600 $\mu$  thick with applied fields of up to 8000 V/cm.

Rhys-Roberts and Tredgold<sup>30</sup> studied BaTiO<sub>3</sub> and found that they could accurately describe the resulting SCLC behavior by introducing the effects of a surface trapping layer. Their current density relationship is

$$J = \frac{(2\pi mKT)^{3/2}}{4\pi h^3 N_o X_1} \frac{V^2}{L^2} \exp\left(\frac{-E_t}{KT}\right) \quad (18)$$

in which the previously undefined symbols  $N_t$  is the trap density of the thin surface layer,  $X_1$  the trapping layer thickness, and  $E_t$  the trap depth in the forbidden region.

Keck<sup>5</sup> found that SCLC occurs in 10 mil thick specimens of polycrystalline BaTiO<sub>3</sub>. His data show a distinct ohmic to SCLC transition. In addition, those samples exhibiting SCLC behavior had the highest tendency to degrade electrically. This provides evidence for a relationship between non-ohmic behavior and degradation.

Although only BaTiO<sub>3</sub> has been cited as an example of a semiconductor exhibiting SCLC behavior, many other insulators ranging from elemental and ionic compounds to vitreous materials exhibit this phenomenon. These are ZnS, CdS, SiC, AlN, and KCl, to name a few.

Several investigators have also closely examined SCLC behavior to extract quantitative information about trap distributions. For example:

Nespurek and Sworakowski<sup>31</sup> developed an analytical method that enables one to extract quantitative information about the energetic distribution of traps from SCLC measurements. They also described the effects of temperature, current instability, and spatial nonuniformity of traps.

Mathur and Dahura<sup>32</sup> developed a distribution that broadly encompasses all the characteristics of the Gaussian distribution and accurately predicts the current density-voltage dependence in the transition region from ohmic to SCLC behavior.

### Summary

The SCLC injection of electrons into insulators is the solid state analog of electron emission from cathode to anode through a vacuum. At low fields, ohmic

behavior is observed with a transition to SCLC at higher fields. The transition field is dependent upon bulk properties of the insulator, namely trap concentration. Traps may be discrete or distributed in some manner. Spatial considerations, such as surface trapping layers, ohmic contact space-charge penetrations, and nonuniformity of trap-distribution, may all play an important role in explaining observed behavior. Valuable information, such as trap distribution and energy depth, is obtainable by making SCLC measurements. This can help yield a defect picture of the insulator being studied.

Four current injection mechanisms have been found to occur in solids. Ohmic injection, Schottky emission, tunneling, and space-charge-limited current. Figure 36 summarizes the insulator thicknesses and applied fields for which each one of these mechanisms apply. The bottom line concerning all of these current injection mechanisms is this: Current technological advances are aimed towards using thinner and thinner dielectrics as active layers in various electronic devices. As thickness decreases and the field increases, a departure from ohmic behavior is more likely, which could have a profound effect upon desired electrical properties. Multilayer capacitors, barrier layer capacitors, varistors, and PTC devices have all been shown to exhibit non-ohmic behavior. In some cases, this deviation results in advantageous properties, whereas in others it limits their capabilities. In any case, in order to elucidate electrical behavior, a thorough knowledge of the various current injection mechanisms found in insulators is needed.

A careful review of the literature has revealed that no concise theory has been developed to explain exactly what happens when current is injected into a material of high permittivity. That is, no attempt has been made to associate observed current injection behavior with polarization mechanisms. Whether this can be related to trapping phenomena is not clear. One of the goals of this study is to develop a relationship describing current injection into high permittivity materials, specifically barium titanate. Of particular interest is the transition region from



Mechanism	Field	Thickness
Ohmic	low	>several mils
Schottky	$10^5$ V/cm	<2 mils
Tunneling	$10^{7-8}$ V/cm	<400 Å
Space - Charge	$10^{3-4}$ V/cm	several mils

Figure 36. Injection Mechanism as Function of Applied Field and Dielectric Thickness.

ohmic to SCLC, which Keck<sup>5</sup> observed in BaTiO<sub>3</sub> polycrystalline samples. Past studies have in general indicated that those samples showing ohmic behavior are less likely to degrade,<sup>5,7</sup> whereas transition to SCLC behavior is detrimental. Much quantitative work needs to be done, with a theory developed to explain the behavior.

#### Thermally Stimulated Current Measurements

Thermally-stimulated polarizations current/thermally stimulated depolarizations current (TSPC/TSDC) measurements have been used extensively to study charge motion in insulators. These measurements are based on the thermally activated release of trapped charges (ions, holes, and electrons) or from polarization mechanisms. If such sources exist in a material, current peaks appear during heating.

The TSPC technique involves measuring the current as the material is subjected to a constant DC field and heated at a constant rate from some low temperature. If the solid contains trapping states, then peaks in the current are observed when the temperature becomes high enough for trapped charge to be released.<sup>33</sup> The current for this process is given by

$$I(T) = A \exp(-E_a/RT) \exp\left[-B \int_T^{T_0} \exp(-E_a/RT) dT\right] \quad (19)$$

in which  $E_a$  is the activation energy or trap depth.  $R$  the Boltzmann constant,  $T_0$  the initial temperature, and  $A$  and  $B$  are constants, which depend upon current source and measurement factors, such as surface area and heating rates.

The TSDC process involves measuring the change released from an already polarized solid as it is heated from a low temperature. During heating, the discharge current results from dipole depolarization and emptying to trapping states.

Because both techniques are very sensitive to trapping states and polarization processes, we believe that the current spectra results coming from the capacitor materials can yield much information regarding the physical and chemical state of the materials. Thus, we have begun to develop the background to evaluate the applicability to TSPC/TSDC techniques to capacitor reliability. Thus, in the following discussion we describe the work that we have done involving the TSPC/TSDC measurements on both laboratory and commercial capacitors.

#### Equipment and Technique

A TSC test chamber is shown in Figure 37. The major components are: (a) copper wire to electrodes, (b) alumina tube, (c) teflon insulation, (d) thermocouple, (e) O-ring, (f) helium inlet, (g) pressure gauge, (h) inner copper tube, (i) thermocouple spaghetti, (j) screw, (k) insulating alumina plate, (l) insulator specimen, (m) metal frame, (n) set screw, (o) electrode, (p) spring, (q) set screw, (r) helium outlet, (s) to vacuum pump, and (t) copper container. The TSC measurement system is electrically isolated from possible RF or electrical interference through the shielding and grounding of the chamber, use of a coax cable, and a battery-operated electrometer. The chamber itself consists of a metal container (stainless steel or copper) with a removable assembly that contains the thermocouples and spring-loaded electrodes. Valved tubes are connected to the metal container to supply the vacuum, inert atmosphere, and exhaust for the interior of the chamber. The vacuum tight chamber can be evacuated by a mechanical pump or back-filled by an inert atmosphere.

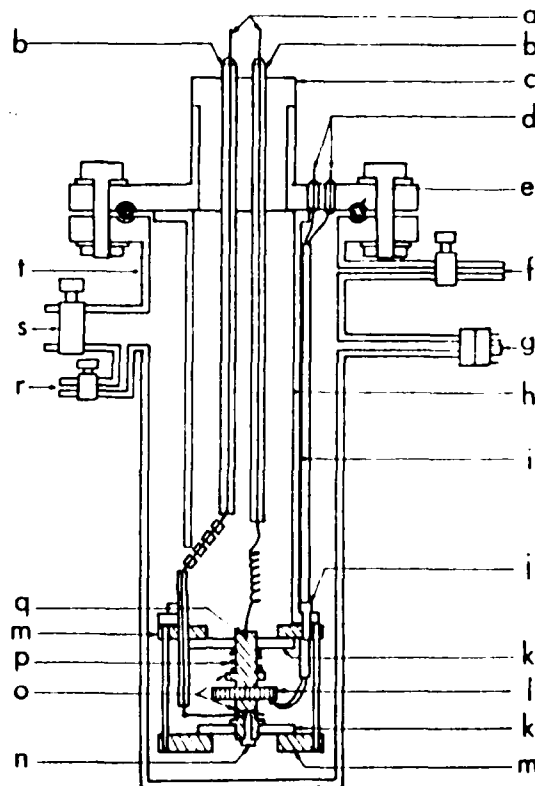


Figure 37. Schematic of Thermally Stimulated Current Specimen Holder and Test Chamber.

A schematic of the measurement circuit is shown in Figure 38. The instruments used in the TSC measurements are a highly-sensitive electrometer (Keithley 602) and a graphic plotter (Linseis L1800). The DC voltage source for making the current measurements of the samples is supplied by batteries. The chamber is heated by heating tape, which is wrapped around the chamber and controlled by a solid state power supply (Eurotherm).

The following is a synopsis of the procedure used in measuring the thermally-stimulated current of a sample:

- a. The sample is placed between the spring-loaded electrodes and inserted into the TSC chamber (electrical leads to instruments connected at this time).

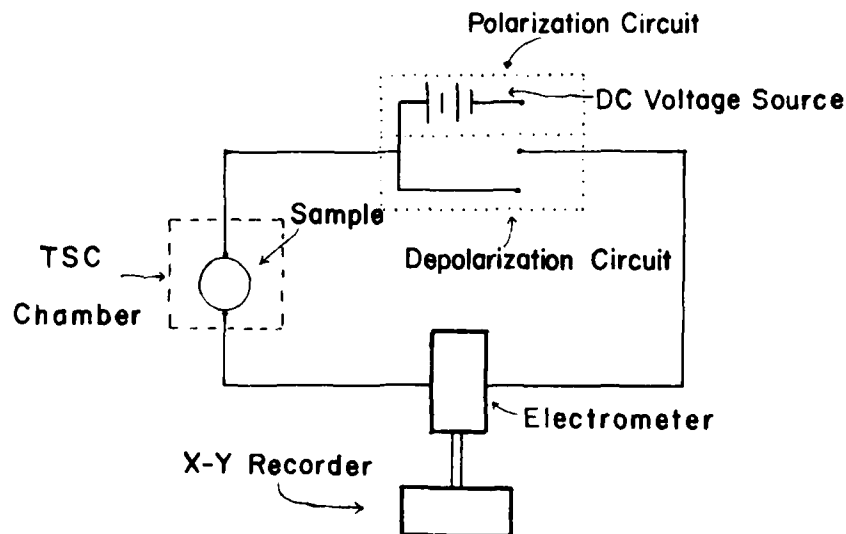


Figure 38. Schematic of Thermally Stimulated Current System.

- b. The sealed chamber is evacuated to around  $10^{-3}$  Torr and heated for 2 to 6 hours to  $165^{\circ}\text{C}$  to aid in removal of moisture from the chamber.
- c. The chamber is then purged with He gas and then is cooled to  $-100^{\circ}\text{C}$  with liquid nitrogen.
- d. After cooling, the sample measurement begins, first by initiating the heating cycle (from  $-100^{\circ}\text{C}$  to  $165^{\circ}\text{C}$  at  $4^{\circ}\text{C}/\text{min}$ . or  $8^{\circ}\text{C}/\text{min}$ ), and second by connecting the voltage source to the system (45 VDC for most of Z5U capacitors and prepared samples, 180 VDC for BX, NPO capacitors).
- e. The electrometer monitors the leakage current (i.e., polarization graph) as the sample is heated.
- f. Once the first polarization measurement is completed (at  $165^{\circ}\text{C}$ ) the sample is cooled to  $100^{\circ}\text{C}$ , and a second polarization run is made. Following the second run, the sample is again cooled to  $100^{\circ}\text{C}$ , the voltage source is removed, and the sample is heated again, this time to measure the depolarization current of the sample.

### TSC Graphs

Figures 29 through 54 show the TSC measurements obtained for a number of prepared samples and commercial capacitors. A list of the graphs is given in Table IV.

**Table IV**

<u>Figure</u>	<u>Sample Description</u>	<u>Polar/Depolar</u>	<u>DC Voltage (polar only)</u>	<u>Heating Cycletime (min.)</u>
39	BaTiO <sub>3</sub> (A/B=1.00)	polar	45	35
40	BaTiO <sub>3</sub> (A/B=1.00)	polar	45	70
41	BaTiO <sub>3</sub> (A/B=1.00)	depolar	-	35
42	BaTiO <sub>3</sub> (A/B=0.97)	polar	45	70
43	BaTiO <sub>3</sub> (A/B=0.97)	depolar	-	70
44	BaTiO <sub>3</sub> (A/B=1.03)	polar	45	70
45	BaTiO <sub>3</sub> (A/B=1.03)	depolar	-	70
46	SrTiO <sub>3</sub>	polar	45	70
47	Al-SrTiO <sub>2</sub>	polar/depolar	180	35
48	LaCrO <sub>3</sub>	polar	45	35
49	TiO <sub>2</sub>	polar/depolar	180	35
50	TiO <sub>2</sub> -Al	polar/depolar	180	35
51	TiO <sub>2</sub> -Nb	polar/depolar	45	35
52	NPO Capacitor	polar/depolar	180	35
53	BX Capacitor	polar/depolar	180	35
54	Z5U Capacitor	polar	180	35

### Figures 39 to 45

All the graphs of both the polarization and depolarization of BaTiO<sub>3</sub> show the three crystallographic structure changes that are normally observed in BaTiO<sub>3</sub>, i.e., first the rhombohedral to orthorhombic transition, then the orthorhombic to tetragonal

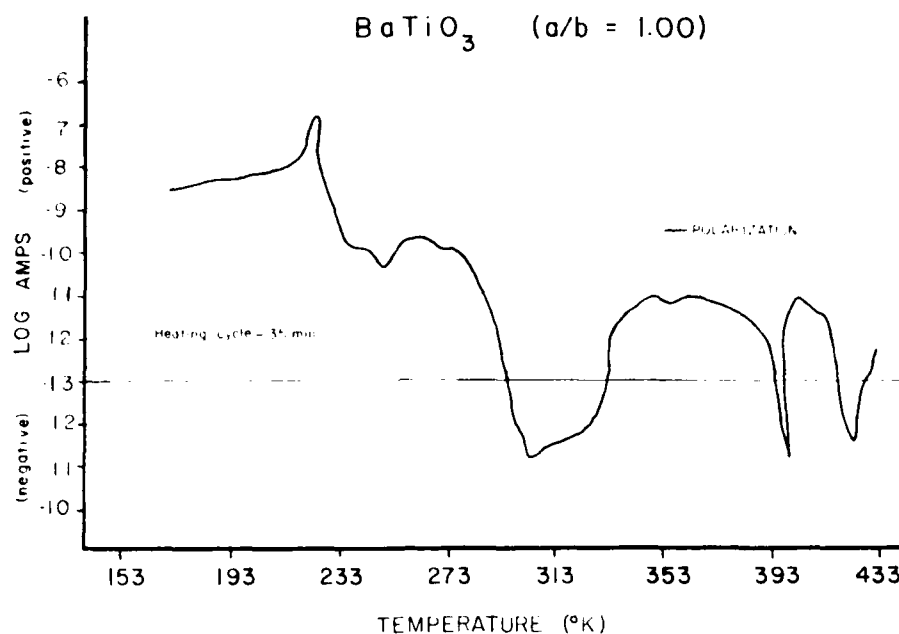


Figure 39. Polarization Current of  $\text{BaTiO}_3$  as Function of Temperature at a Field of 100 kV/m and Heating Rate of 0.13  $^{\circ}\text{K/s}$ .

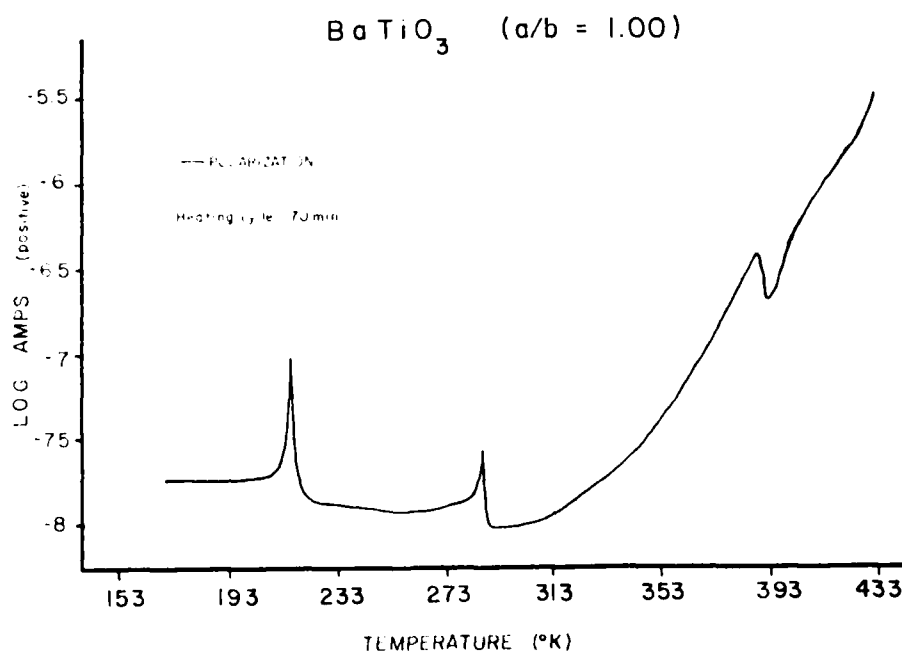


Figure 40. Polarization Current for  $\text{BaTiO}_3$  as Function of temperature at a Field of 100 kV/m and Heating Rate of 0.07  $^{\circ}\text{K/s}$ .

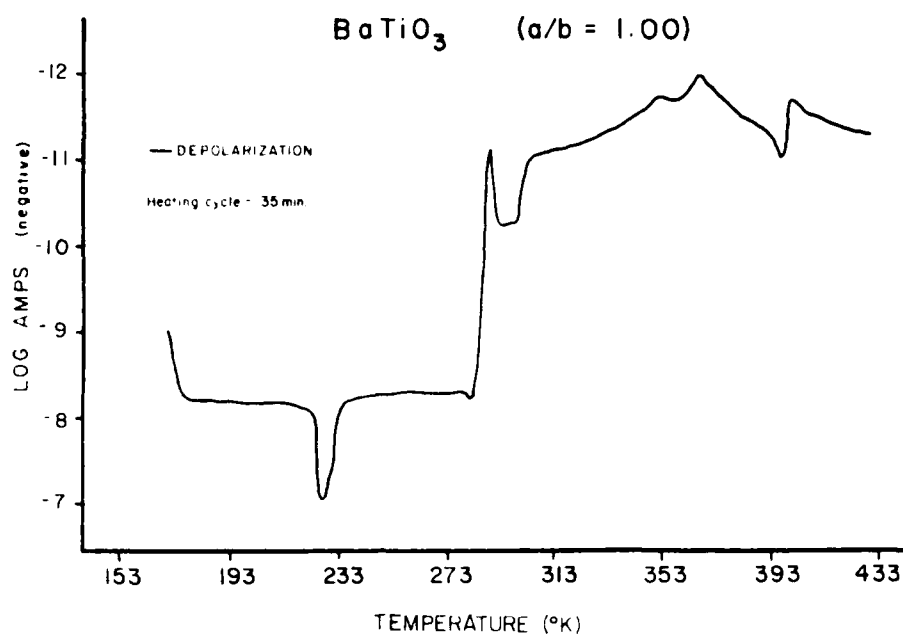


Figure 41. Depolarization Current for  $\text{BaTiO}_3$  as Function of Temperature with Field of 100 kV/m and Heating Rate of 0.13 °K/s.

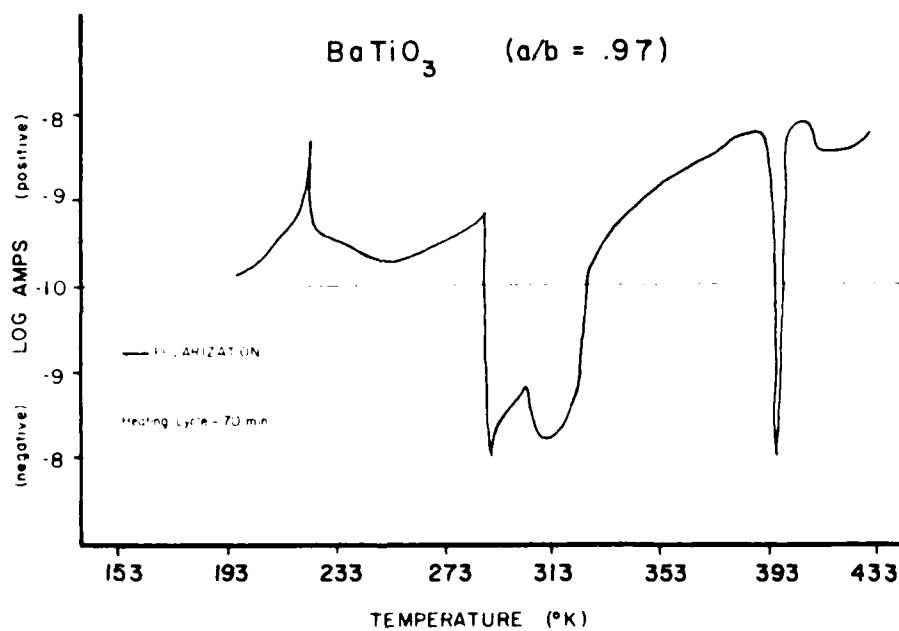


Figure 42. Polarization Current for  $\text{Ba}_{.97}\text{TiO}_3$  as Function of Temperature with Field of 100 kV/m and Heating Rate of 0.07 °K/s.

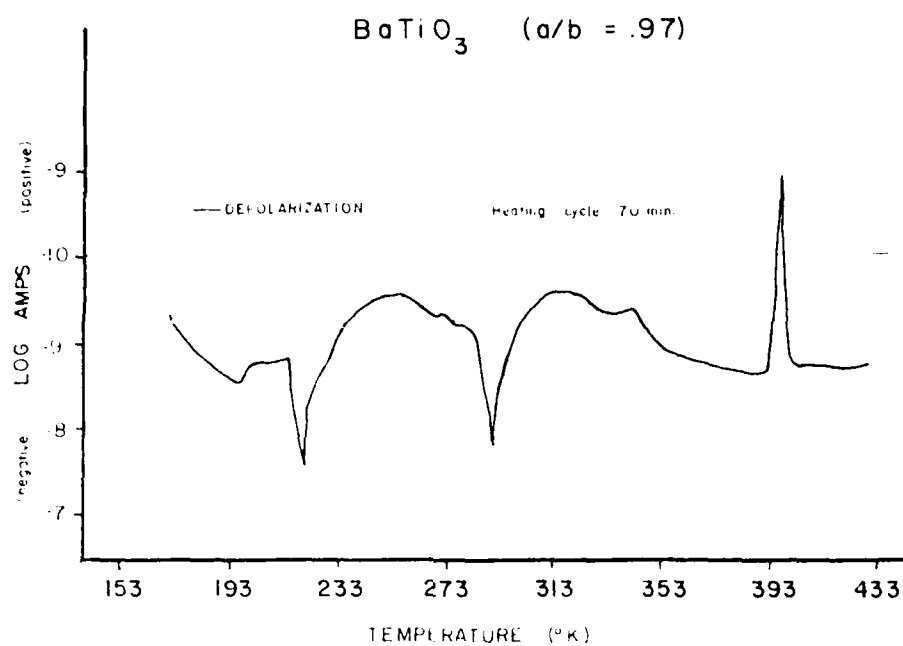


Figure 43. Depolarization Current of  $\text{Ba}_{.97}\text{TiO}_3$  as Function of Temperature with Field of 100 kV/m and Heating Rate of 0.07  $^{\circ}\text{K/s}$ .

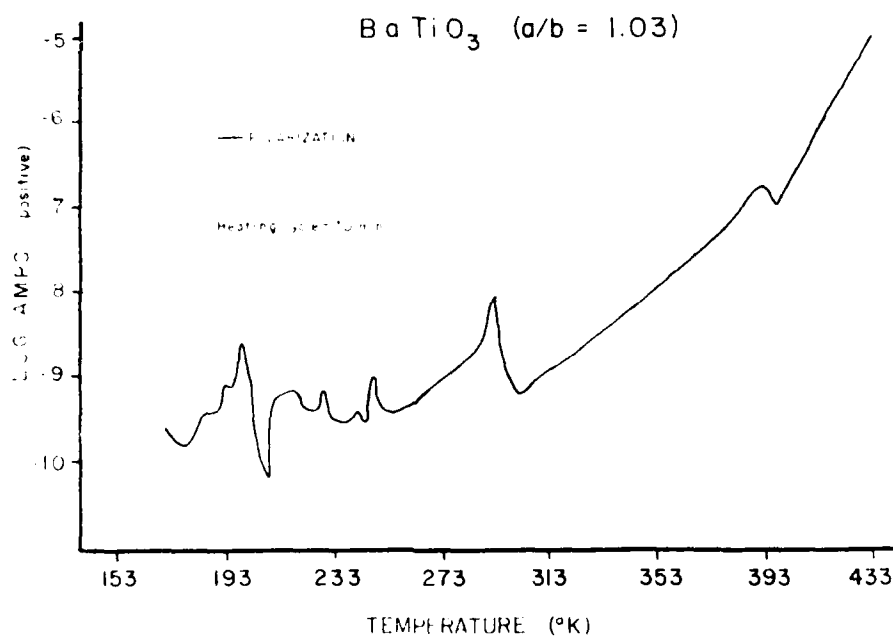


Figure 44. Polarization Current of  $\text{Ba}_{1.03}\text{TiO}_3$  as Function of Temperature with Field of 100 kV/m and Heating Rate of 0.07  $^{\circ}\text{K/s}$ .



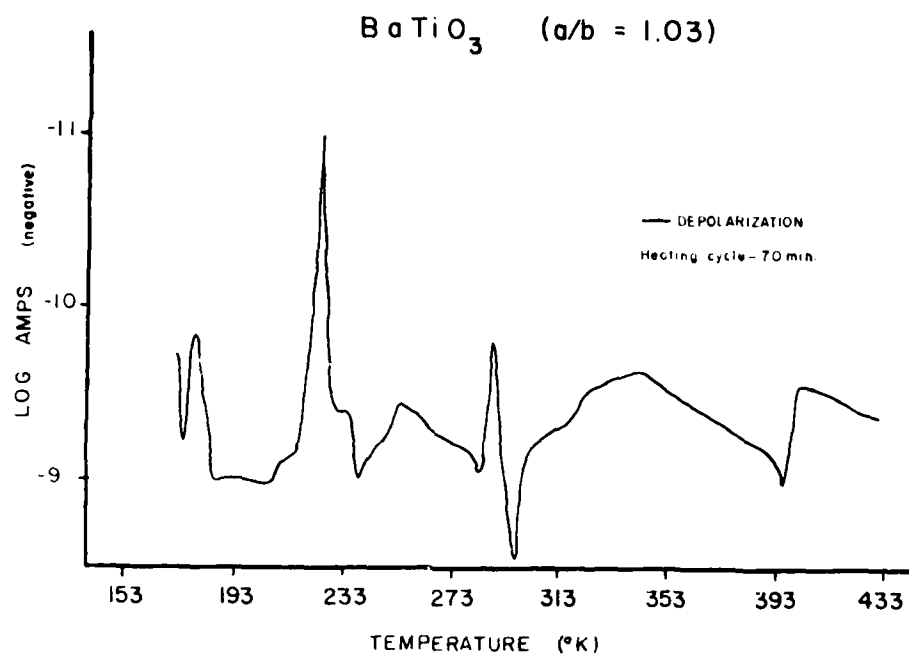


Figure 45. Depolarization Current of  $\text{Ba}_{1.03}\text{TiO}_3$  as Function of Temperature with a Field of 100 kV/m and Heating Rate of 0.07  $^{\circ}\text{K/s}$ .

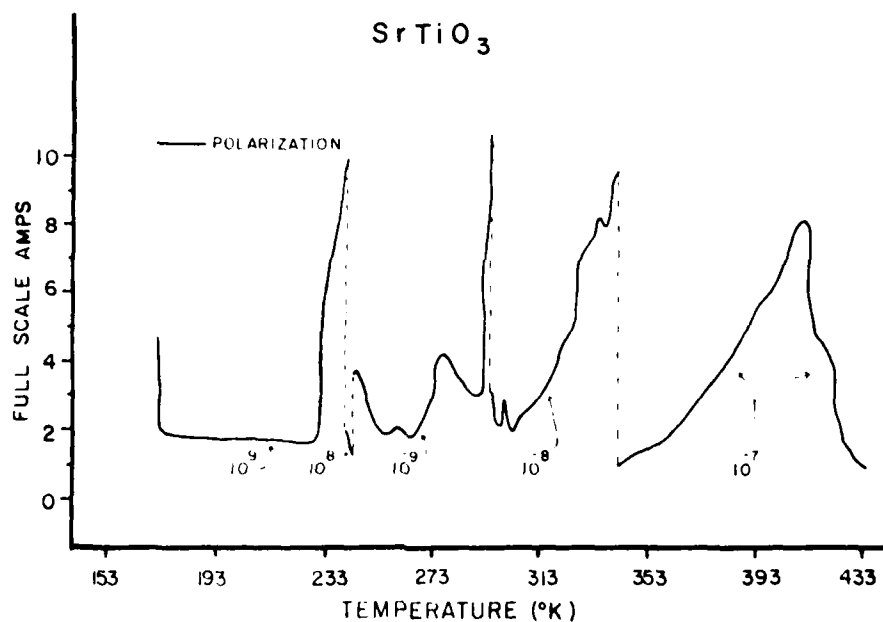


Figure 46. Polarization Current for  $\text{SrTiO}_3$  Single Crystal as Function of Temperature with Field of 200 kV/m and Heating Rate of 0.13  $^{\circ}\text{K/s}$ .

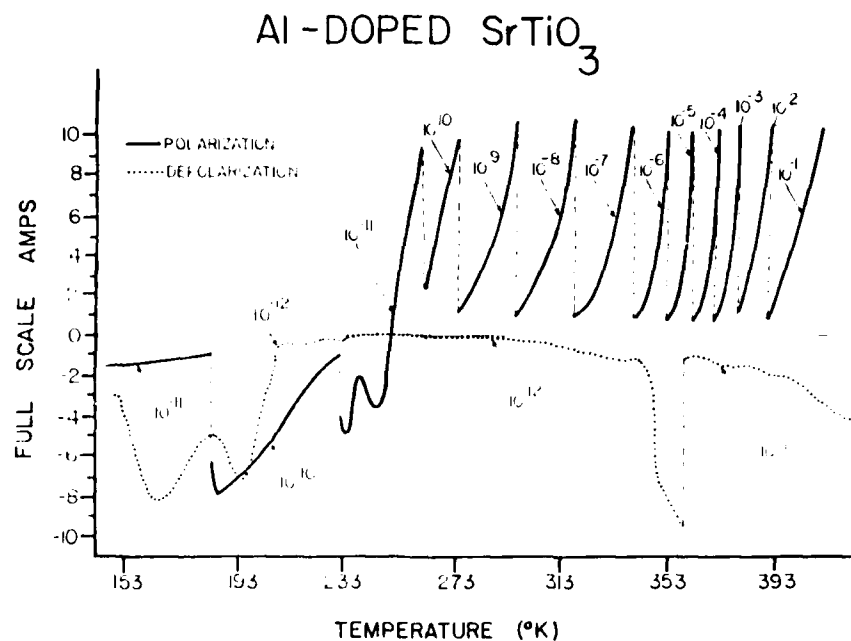


Figure 47. Polarization and Depolarization Currents for Al Doped  $\text{SrTiO}_3$  Single Crystals as Function of Temperature with Polarization Field of 200 kV/m and Heating Rate of 0.13  $^{\circ}\text{K/s}$ .

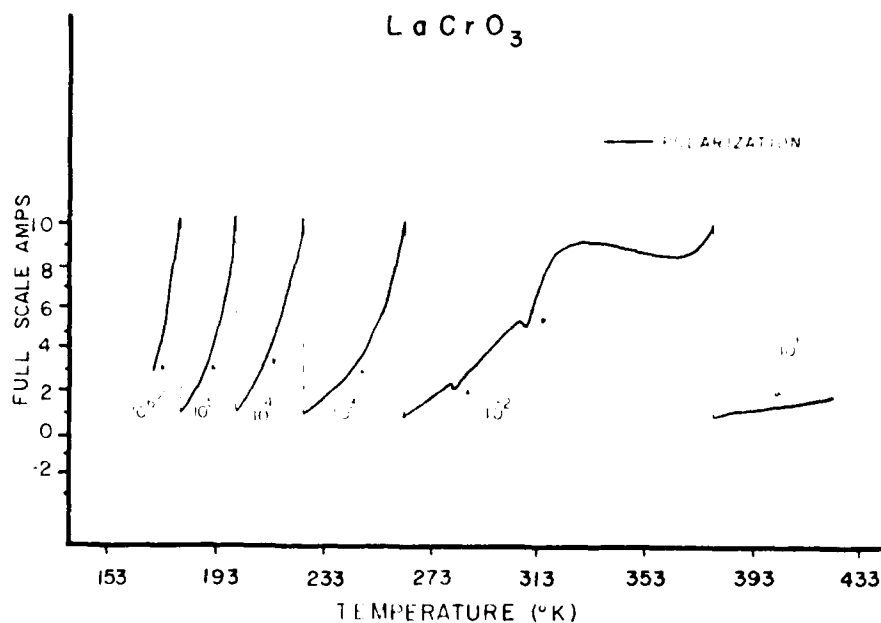


Figure 48. Polarization Current for  $\text{LaCrO}_3$  as Function of Temperature at a Field of 100 kV/m and Heating Rate of 0.13  $^{\circ}\text{K/s}$ .

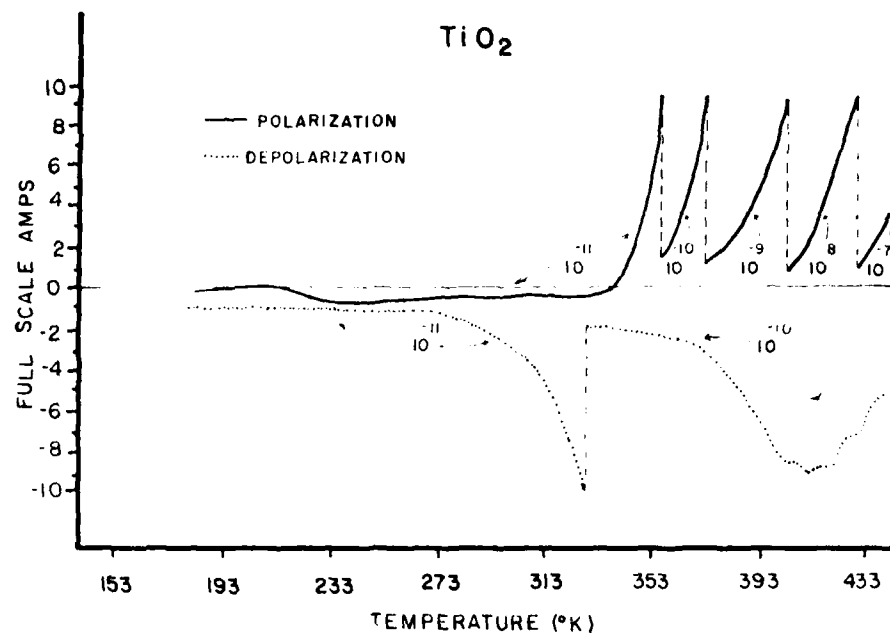


Figure 49. Polarization and Depolarization Currents for Single Crystal  $\text{TiO}_2$  as Function of Temperature at Polarization Fields of 200 kV/m and Heating Rate of 0.13 °K/s.

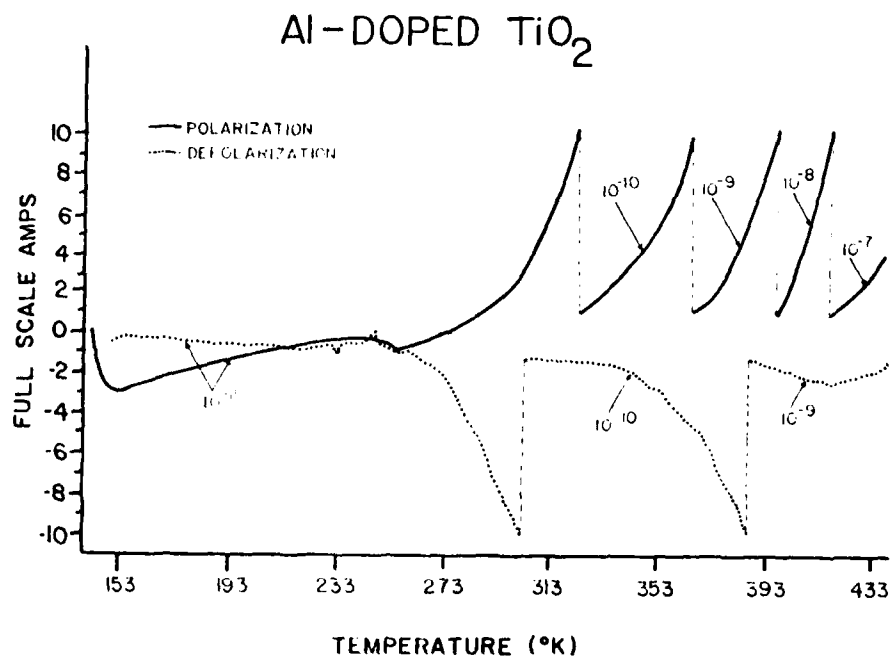


Figure 50. Function of Temperature for Al Doped  $\text{TiO}_2$  Single Crystal for Polarization Fields of 200 kV/m and Heating Rate of 0.13 °K/s.

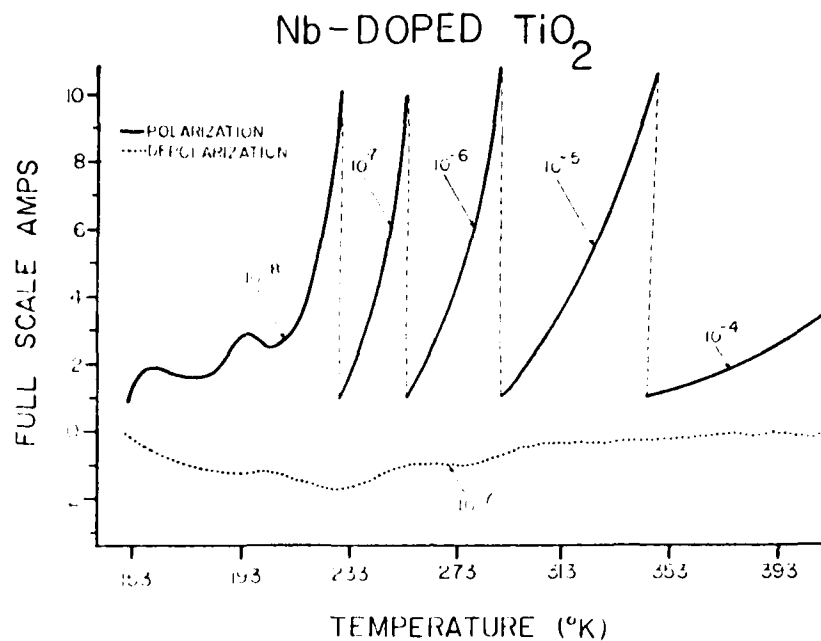


Figure 51. Polarization and Depolarization Currents as Function of Temperature for Nb-Doped  $\text{TiO}_2$  Single Crystal at Fields of 100 kV/m and Heating Rate of 0.13  $^{\circ}\text{K/s}$ .

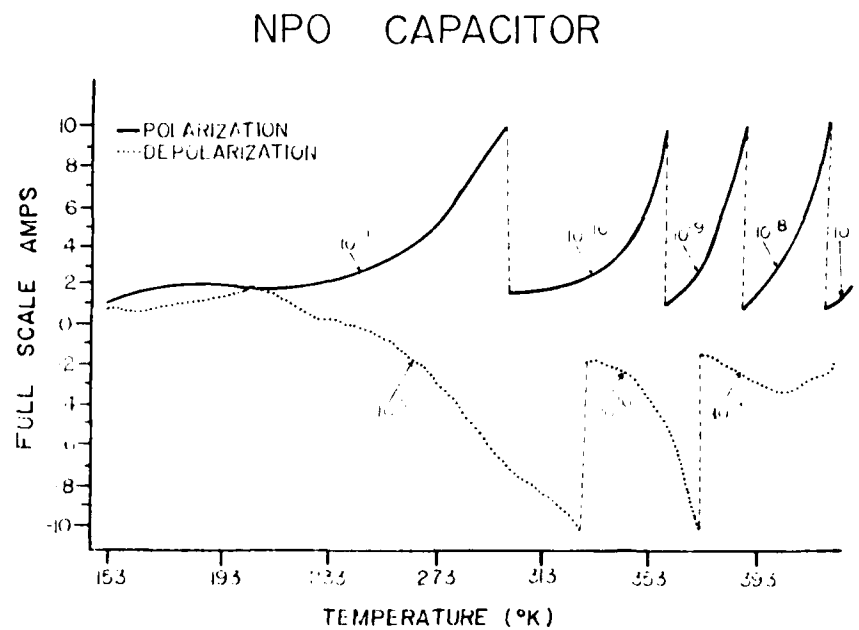


Figure 52. Polarization and Depolarization Current as Function of Temperature for a Multilayer NPO Capacitor for a Polarization Field of 720 kV/m and Heating Rate of 0.13  $^{\circ}\text{K/s}$ .

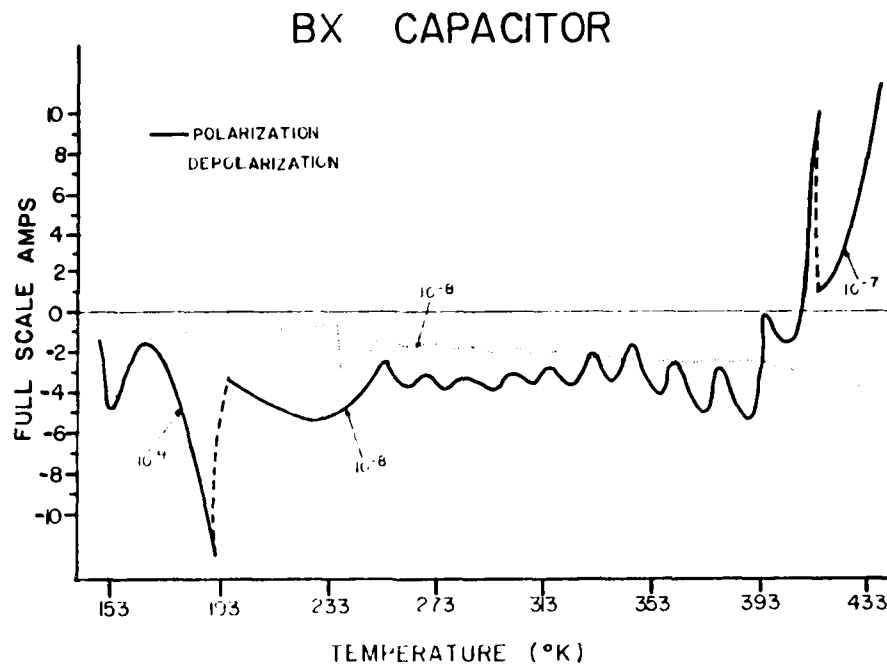


Figure 53. Polarization and Depolarization Currents as Function of Temperature for a BX Multilayer Capacitor for a Polarization Field of 720 kV/m and Heating Rate of 0.13 °K/s.

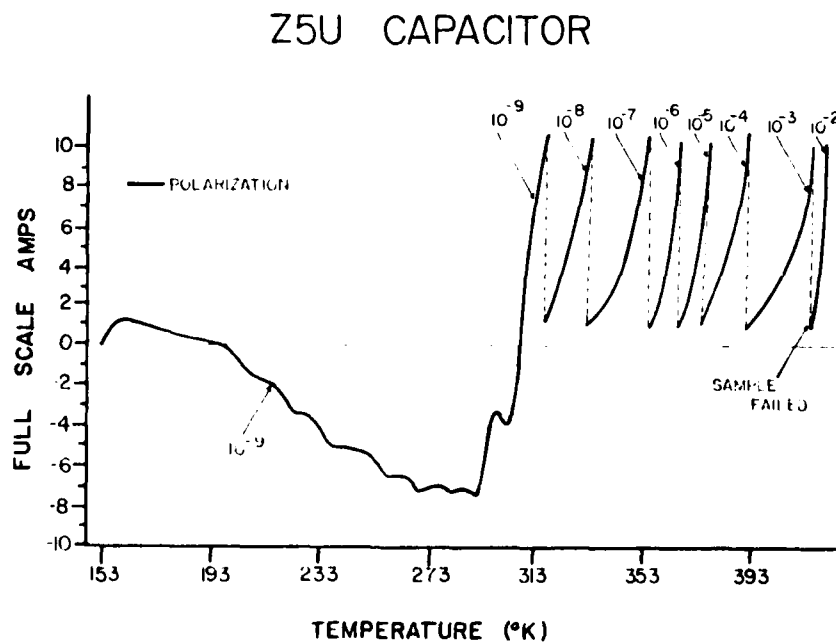


Figure 54. Polarization Current as Function of Temperature for a Z5U Multilayer Capacitor with a Field of 180 kV/m and Heating Rate of 0.13 °K/s.

transition, and finally the tetragonal to cubic transition). The graphs of  $\text{BaTiO}_3$  at A/B ratios of 1.00 and 0.97 (polar and depolar) show a negative to positive leakage current transition or a positive to negative leakage above and below the Curie temperature. The specific exceptions to this are the graphs of  $\text{BaTiO}_3$  at A/B ratio of 1.03 (Figs. 44,45) and the graphs of  $\text{BaTiO}_3$  at A/B ratio of 1.00 (Figs. 38-40) with a 70 minute cycle time in which no negative to positive current transition is seen. Also to be seen in these exceptions is that the leakage current in the polarization graphs are the highest recorded among the  $\text{BaTiO}_3$  samples measured. This indicates that these samples are possibly becoming more conductive and might eventually fail.

The graphs for  $\text{SrTiO}_3$  (Fig. 46) and  $\text{TiO}_2$  (Fig. 49) show some low temperature change absorption but in general depict behavior that can be attributed to a paraelectric behavior. That is, no pattern changes or temperature correlated polarizations are observed. The curve for  $\text{LaCrO}_3$  (Fig. 48) is an illustration of the polarization of an electronic conductor in which no polarization occurs, only leakage current. That is, the specimen is so conducting that no net charge storage can be observed.

The size of the tetrahedral-cubic transition peak and the magnitude of the current below and above the transition appears to be cation stoichiometric dependent. The magnitude of the peak is probably related to the particular current injection mechanism prevalent in the particular composition. Previous data have shown that for  $\text{Ba/Ti} > 1.000$ , most materials behave ohmically, but for  $\text{Ba/Ti} \leq 1.000$ , space charge limited current prevails. The significance of this with regard to the TSPC current is that the current is proportional to the dielectric constant (see Eq. (11)).

Figure 55 illustrates the behavior of the dielectric constant for  $\text{Ba/Ti} = 0.995$ . The important features at a field of 0.1 kVAC/cm are the classic behavior of the ferroelectric-paraelectric transition with Curie-Weiss behavior in the paraelectric state. The Curie-Weiss law is

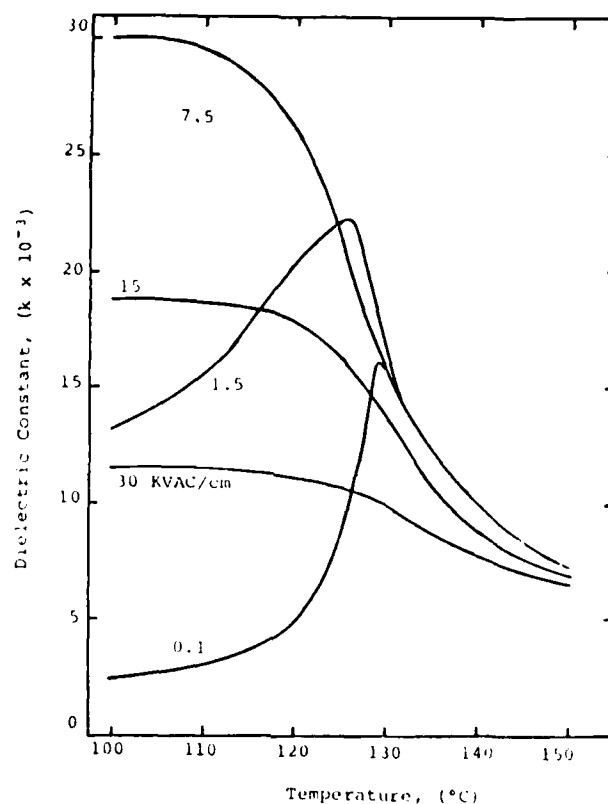


Figure 55. Dielectric Constant vs. Temperature Behavior at Different Applied Fields for Undoped Barium Titanate, Ba:Ti = 0.995.

$$K = C_0/(T-T_0) \quad (20)$$

in which  $K$  is the dielectric constant,  $C_0$  the Curie constant,  $T$  the temperature, and  $T_0$  the Curie temperature. Increasing the field increases the dielectric constant in the ferroelectric state to a maximum value at a field of about 7.5 kVAC/cm. The dielectric behavior in the paraelectric state is independent of the field. Increasing the field to levels greater than 7.5 kVAC/cm decreases the dielectric constant in both the ferroelectric and paraelectric phases and, as can be observed, the change in the dielectric constant during the transition becomes more gradual.

In general, the dielectric behavior of other compositions is similar to that observed for the Ba/Ti = 0.995. The only differences are in the measured dielectric constant, in the field that maximizes the dielectric constant in the cubic state, and

the abruptness of the change in the dielectric constant during the transition at different fields.

The current characteristics are determined by applying the DC field at about 110°C and heating through the transition temperature at a rate of about 1°C/min. The temperature is increased immediately after the field is applied and long time charging effects are ignored.

Figure 56 illustrates the current vs. temperature curves for Ba/Ti = 0.995 at 1.97 and 3.94 kVDC/cm. At 1.97 kVDC/cm, the current flow reverses direction and

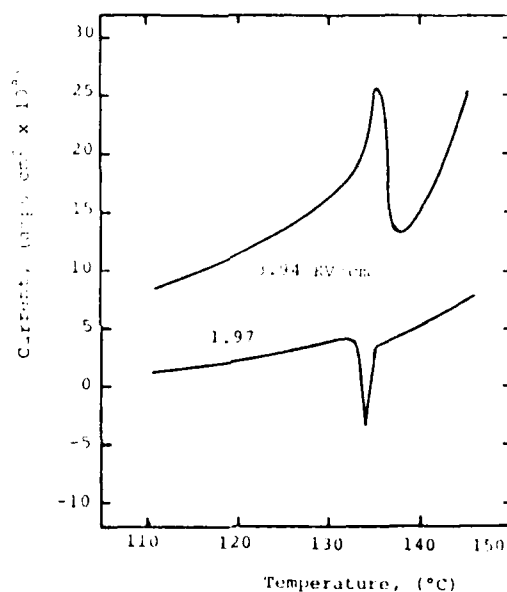


Figure 56. Measured Current for Undoped Barium Titanate, Ba:Ti = 0.995, at a Heating Rate of 1°C/min at Different Applied Fields.

is negative for a brief period. After the transition, the curve is displaced to a lower level than in the ferroelectric state. At 3.94 kVDC/cm, the current increases during the transition and then decreases to a lower level. The difference of current levels in the ferroelectric and paraelectric regions can be explained by the temperature dependence of the dielectric constant. Because of the lower dielectric constant in the paraelectric state, the current should be lower than that in the ferroelectric



region; however, the change in current is much less than that predicted by the change in the dielectric constant. This indicates that the simple model presented for space-charge-limited current does not adequately describe this system.

The behavior during the transition can be explained by considering the sample as a capacitor in parallel with a resistor. The behavior of the capacitor is of importance. The charge per unit area,  $Q$ , on a capacitor is

$$Q = CV \quad (21)$$

in which  $C$  is the capacitance per unit area, and  $V$  the voltage. The capacitance per unit area is

$$C = \frac{\epsilon_0 K}{\ell} \quad (22)$$

in which  $\ell$  is the electrode spacing. By combining Eqs. (21) and (22), one obtains

$$Q = kV\epsilon_0/\ell. \quad (23)$$

The current flowing in the capacitor,  $J_C$ , is obtained by taking the first derivative of Eq. (23) with respect to time,  $t$ , which is

$$J_C = d(kV\epsilon_0/\ell)/dt. \quad (24)$$

The only variable, which depends upon time in Eq. (24), is the dielectric constant, because the dielectric constant is a function of temperature, and the temperature is a function of time related to the constant heating rate. Introducing temperature by the chain rule, Eq. (24) becomes:

$$J_C = (V\epsilon_0/\ell) (\partial k/\partial T) (\partial T/\partial t) \quad (25)$$

in which  $\partial k/\partial T$  is the slope of the dielectric constant vs. the temperature curve at the applied field,  $V/\ell$ , and  $\partial T/\partial t$  the heating rate. This capacitance current must be subtracted from the resistance current flowing through the sample because it is in the opposite direction.

The capacitance current would be maximized by a high temperature dependence of the dielectric constant and a high heating rate. With regard to Figure 54, the

greatest temperature dependence is at fields from about 1 kVAC/cm (0.5 kVDC/cm) to about 10 kVAC/cm (5 kVDC/cm). Because the sample is not at thermal equilibrium, the transition occurs over a greater time period and reduces the equilibrium temperature dependence. By using values of 2 kVDC/cm,  $10^3/^{\circ}\text{C}$ , and  $1^{\circ}\text{C}/\text{sec}$ , the calculated value of  $J_c$  of  $1.8 \times 10^{-7} \text{ amp}/\text{cm}^2$  can be compared well with the measured value of  $7.5 \times 10^{-8} \text{ amp}/\text{cm}^2$ . The transition behavior with a field of 3.94 kVDC/cm is probably a function of the dielectric constant dependence of both space-charge-limited behavior and of capacitance.

Figure 57 illustrates the current vs. temperature plot at 1.97 and 3.94 kVDC/cm for Ba/Ti = 1.005. There is no change during the ferroelectric-paraelectric transition at 0.98 kVDC/cm. At 3.94 kVDC/cm, there is a small change during the transition.

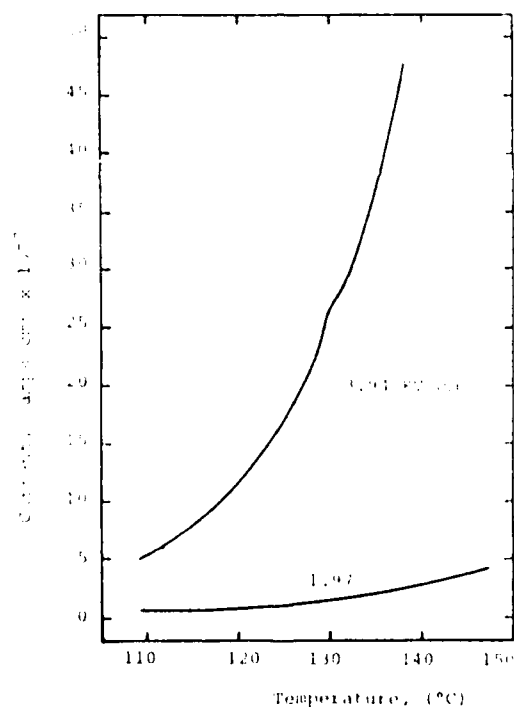


Figure 57. Measured Current for Undoped Barium Titanate, Ba:Ti = 1.005, at a Heating Rate of  $1^{\circ}\text{C}/\text{min}$  at Different Applied Fields.

The change in the dielectric constant during the transition is more gradual with this composition than when  $\text{Ba/Ti} = 0.995$  (Fig. 45). Because this composition does not display space-charge-limited current, there is no change in the current resulting from the change in the dielectric constant.

Figures 52 to 54 depict the TSC graphs for the NPO, BX, and Z5U capacitors. As expected, the NPO capacitor behaves similarly to the  $\text{TiO}_2$  (Figs. 49,50) because it is paraelectric. The BX capacitor spectrum shows basic similarities to the  $\text{BaTiO}_3$  curves with a peak at the Curie point and increasing leakage current above the Curie point. In this case, the Curie point shifts downward (in temperature) and is depressed (in magnitude) from the addition of various additives (possibly  $\text{SrTiO}_3$  to shift,  $\text{Bi}_2\text{O}_3$  to depress, as examples). Again, in the Z5U capacitor graph, the similarities are to  $\text{BaTiO}_3$  with the Curie point shifted possibly by  $\text{SrTiO}_3$ , but the most noticeable difference being the dramatic increase in current at temperatures above the Curie point. Because of this, Z5U capacitors are used mainly for low voltage and room temperature applications (compared to BX and NPO capacitors), although higher capacitance can be achieved with Z5U capacitors. It is apparent that the compositional inhomogeneities in both the BX and Z5U capacitor formulations, which are required to give the correct TCC, also lead to a rather complicated TSPC/TSDC current spectrum. A broad range of Curie points can be seen in the current spectrum of each. Being able to observe such localized nonhomogeneities with the TSPC/TSDC technique is encouraging and leads us to believe that both physical as well as chemical defects (or irregularities) can be detected by this measurement.

### Conclusion

In general, the TSPC/TSDC curves show an extreme sensitivity to polarization mechanisms and can detect small changes in polarization processes, which cannot be observed by either electrical conductivity or capacitance measurements. It is

also apparent that this technique can readily distinguish between the various capacitation types: NPO, Z5U, and BX, for example. Thus, our work involving TSPC/TSDC measurements is being continued and expanded.

### **COOPERATIVE PROGRAMS**

#### **University of Missouri-Rolla/Draper Laboratory Program**

In June, we embarked on a test program with Draper Laboratories (Robbins). In this program, Draper is obtaining a number of leaded and chip capacitors from commercial vendors. These capacitors cover a wide range of capacitances with NPO, X7R, and Z5U characteristics.

Draper is retaining half of the units and is sending us the other half (mainly leaded).

The intent of the program is to 1) screen all of the capacitors with the methanol test, 2) test a representative sampling of both units, which pass the methanol test and those which fail, by using the 85/85/1.5VDC test and determine the TSC spectrum of each, 3) compare the test results on similar units, 4) do destructive testing on units that display low voltage failure, and 5) make degradation measurements on both "good" and "bad" units to determine the I-V profile and temperature dependence of the leakage current.

This program is well on its way, and we expect to report the results in March 1984 at the components meeting (CARTS). Currently, we are conducting the program as part of our Office of Naval Research (ONR) program with no additional funds from Draper. If it expands beyond its present scope, we will expect additional support from Draper.

#### **University of Missouri-Rolla/Pennsylvania State University Program**

Early in our ONR program, we established a relationship with the Dielectrics Center at the Materials Research Laboratory at Pennsylvania State University (PSU) in which we agreed to share specimens and assist each other in carrying out

reliability and thermally stimulated current studies. To this end the following has occurred:

1. Over the past year UMR and PSU personnel have met on three occasions to discuss progress and future directions.
2. UMR has provided PSU with high purity  $\text{BaCO}_3$  and  $\text{SrCO}_3$ .
3. PSU and UMR have exchanged specimens on which TSC measurements have been made by each. This has been done to compare results obtained through different test techniques.
4. UMR and PSU have agreed to coordinate the graduate programs of Wayne Huebner (UMR) and Dean Anderson (PSU). It is the intent for the two studies to be made on the same or as nearly identical specimens as possible so that results can be compared. This will also give both students the opportunity to make use of the strengths of UMR and PSU. For example, it is intended that UMR will prepare much of the powder, and PSU will fabricate the multilayers.

This interaction is well underway and, hopefully, will lead to studies which complement each other.

## REFERENCES

1. M. Pechini, U. S. Patent 3330697, July 1967.
2. K. Kiss, J. Magder, M. S. Vukosovich, and R. T. Lockhart, J. Am. Cer. Soc. 49 291 (1966).
3. K. Mazdivasni, R. Dolloff, and J. Smith, J. Am. Cer. Soc. 52 523 (1969).
4. C. Marcilly, P. Courly, and B. Delmon, J. Am. Cer. Soc. 53 56 (1970).
5. J. Keck, "Electrical Degradation of High Purity Barium Titanate", Ph.D. Dissertation, Univ. Mo.-Rolla, 1976.
6. R. C. Chittick, F. Grey, J. H. Alexander, M. P. Drake, and E. L. Bush, Proc. 3rd Capacitor and Resistor Technology Symp., p. 61, March 8-10, 1983.
7. Hickmott, T. W., J. Appl. Phys., 51 4269 (1980).
8. Emtage, P. and Tantraporn, N., Phys. Rev. Letters, 8 267, 4/1962.
9. Lengyel, G., J. Appl. Phys., 37 807 (1966).
10. Tantraporn, W., and Harris.
11. Haeskeylo, M., J. Appl. Phys., 35 2943 (1964).
12. Payne, D., "Concerning the Physics of Failure of Barium Titanate Capacitors", Proceedings of the Sixth Annual Reliability Physics Symposium, Los Angeles (1967).
13. Johansen, I. T., J. Appl. Phys., 37 499 (1966).
14. Chynoweth, A., Progress in Semiconductors, Vol. 4, 97-123, John Wiley and Sons, Inc., New York (1960).
15. Fisher, J., and Glaever, L., J. Appl. Phys., 32 172 (1961).
16. Ekrut, H. and Hahn, A., J. Appl. Phys., 51 1686 (1980).
17. Maserjian, J., and Zamani, N., J. Appl. Phys., 53 559 (1982).
18. Matsuoka, M., "Progress in Research and Development of ZnO Varistors", Grain Boundary Phenomena in Electronic Ceramics, Vol. 1, pp. 290-308, The American Ceramic Society (1981).
19. Child, C. D., Phys. Rev., 32 492 (1911).
20. Mott, N. F. and Gurney, R. W., Electronic Processes in Ionic Crystals, Oxford Univ. Press, London 1940.
21. Rose, A., Phys. Rev., 97 15 (1955).
22. Lampert, M. and Mark, P., Current Injection in Solids, Academic Press, New York (1970).

23. Ruppel, W., *Helv. Phys. Acta*, 31 311 (1958).
24. O'Reilly, T. J., DeLucia, J., *Sol. State Electronics*, 18 965 (1975).
25. Rosenthal, A. and Sagar, A., *J. Appl. Phys.*, 45 2787 (1974).
26. Edwards, D. A., and Jones, P. L., *Sol. State Electronics*, 21 1163 (1978).
27. Smith, R. and Rose, A., *Phys. Rev.*, 97 1531 (1955).
28. Branwood, A. and Tredgold, R., *Proc. Phys. Soc.*, 76 93 (1960).
29. Branwood, A., Hughes, O. H., Hurd, J. D., and Tredgold, R. H., *Proc. Phys. Soc.*, 79 1161 (1962).
30. Rhys-Roberts, C. and Tredgold, R., *Proc. Phys. Soc.*, 76 497 (1960).
31. Nespurek, S. and Sworakowski, J., *J. Appl. Phys.* 51 2098 (1980).
32. Mathur, V. and Dahura, K., *Sol. State Elec.* 42 61 (1974).
33. Hong, C. and Day, D., *J. Matl. Sci.*, 14 493 (1979).

